chemengineering

MDPI

Article

Enhancement of Photocatalytic Activity and Microstructural Growth of Cobalt-Substituted $Ba_{1-x}Co_xTiO_3$ {x = 0, . . . , 1} Heterostructure

Sana Jebali, Mahdi Meftah, Chadha Mejri, Abdesslem Ben Haj Amara and Walid Oueslati *

LR19ES20: Resources, Materials and Ecosystems (RME), Faculty of Sciences of Bizerte, University of Carthage, Bizerte 7021, Tunisia

* Correspondence: walidoueslati@ymail.com; Tel.: +216-22-144-337

Abstract: The photocatalytic degradation process and absorption kinetics of the aqueous solution of the Cibacron Brilliant Yellow 3G-P dye (Y) were investigated under UV-Vis light. Pure barium titanate $BaTiO_3$ (BT) and cobalt ion-substituted barium $Ba_{1-x}Co_xTiO_3$ (x = 0, . . . , 1) nano-compound powders (BCT) were synthesized using the sol–gel method and colloidal solution destabilization, and utilized as photocatalysts. The powder X-ray diffraction (PXRD) crystal structure analysis of the BT nanoparticles (NPs) revealed a prominent reflection corresponding to the perovskite structure. However, impurities and secondary phase distributions were qualitatively identified in the PXRD patterns for $x \geq 0.2$ of cobalt substitution rate. Rietveld refinements of the PXRD data showed that the BCT nano-compound series undergoes a transition from perovskite structure to isomorphous ilmenite-type rhombohedral $CoTiO_3$ (CT) ceramic. The nanoparticles produced displayed robust chemical interactions, according to a Fourier transform infrared spectroscopy (FTIR) analysis. The BT and BCT nanoparticles had secondary hexagonal phases that matched the PXRD results and small aggregated, more spherically shaped particles with sizes ranging from 30 to 114 nm, according to transmission electron microscopy (TEM). Following a thorough evaluation of BCT nano-compounds with (x = 0.6), energy-dispersive X-ray (EDX) compositional elemental analysis revealed random distributions of cobalt ions. Through optical analysis of the photoluminescence spectra (PL), the electronic structure, charge carriers, defects, and energy transfer mechanisms of the compounds were examined. Due to the cobalt ions being present in the BT lattice, the UV-visible absorption spectra of BCT showed a little red-shift in the absorption curves when compared to pure BT samples. The electrical and optical characteristics of materials, such as their photon absorption coefficient, can be gathered from their UV-visible spectra. The photocatalytic reaction is brought about by the electron–hole pairs produced by this absorption. The estimated band gap energies of the examined compounds, which are in the range of 3.79 to 2.89 eV, are intriguing and require more investigation into their potential as UV photocatalysts. These nano-ceramics might be able to handle issues with pollution and impurities, such as the breakdown of organic contaminants and the production of hydrogen from water.

Keywords: barium titanate; perovskite structure; cobalt substitution; sol–gel process; photocatalytic activity

Citation: Jebali, S.; Meftah, M.; Mejri, C.; Ben Haj Amara, A.; Oueslati, W. Enhancement of Photocatalytic Activity and Microstructural Growth of Cobalt-Substituted $Ba_{1-x}Co_xTiO_3$ {x = 0, . . . , 1} Heterostructure. *ChemEngineering* **2023**, *7*, 43. https://doi.org/10.3390/chemengineering7030043

Academic Editors: Alírio E. Rodrigues, Vicente Montes, Rafael Estevez and Manuel Checa

Received: 24 February 2023
Revised: 20 April 2023
Accepted: 21 April 2023
Published: 1 May 2023

1. Introduction

The generation of contaminated wastewater during manufacturing and industrial processes [1] poses a significant threat to natural waterways and the purity of finite aquifers [2]. Many industrial waste products [3,4] also contain toxic substances that pollute the environment and exacerbate existing health problems [5]. The textile industry contributes to substantial environmental problems due to the effluent flows that contain dyes [6]. Reactive dyes, such Cibacron Brilliant Yellow 3G-P (Y), are widely used in dyestuffs due to their useful qualities, such as bright colors, water-fastness, and less energy usage during

the dyeing process [7]. However, these dyes are extremely reactive and might adversely affect the environment [8]. These characteristics are crucial for preserving the purity of streamflow since even trace levels of highly reactive colorants may generate undesirable water discoloration as well as potentially disastrous impacts on the waterway and the biosystem [9]. Therefore, a solution is required to remove textile dyes from effluents and reduce the toxicity, mutagenicity, and carcinogenicity of reactive dyes and their breakdown products. To remove textile colors from industrial effluents, a variety of approaches are being investigated [10]. One promising method is the use of advanced oxidation processes (AOPs), which can provide efficient dye removal [11,12]. The photocatalytic degradation process, which employs nanoparticles as photocatalysts, has been shown to be a low-cost, highly efficient, and photostable process [13,14]. The key benefit of the photocatalytic process is its ability to remove a wide range of pollutants from contaminated water without leaving behind hazardous residues [15].

Due to their significance in both device applications and fundamental science, multiferroic materials [16], particularly those based on perovskite systems, have undergone a tremendous growth in research and development in recent years [17,18]. These materials make good candidates for research because they have the crucial attribute of composition and morphology adjustability. Various methods, such as doping [19–25], mixing [26,27], substituting [28–37], and fusing [38] can be employed to modify these heterostructure compounds.

Research into the $BaTiO_3$-$CoTiO_3$ system's phase transition as the level of Ba substitution increases, as well as the optical properties of the hole's edge brought on by cobalt substitution on the $BaTiO_3$ A-site, is still relatively new and underdeveloped. By examining variations in the optical characteristics and phase transition behavior of (cobalt/barium) titanium oxide (BCT), this study intends to optimize and improve photocatalytic properties. The results of this research could have a big impact on the creation of cobalt-substitution-based photocatalytic materials that are more effective and efficient. This study aims to increase the degradation efficiency and absorption kinetics of the Cibacron Brilliant Yellow 3G-P dye under well-quantified visible and UV irradiation [7,9,39–41]. Recently, perovskite oxides with the ABO_3 crystal structure have been proposed as efficient bifunctional electrocatalysts due to their low cost, flexible electrocatalytic capabilities, and improved performance in reaction-related applications [42,43]. Less symmetrical structures are observed when the ionic radius decreases, as the Goldschmidt tolerance factor is reduced. The octahedral BO_6 experiences distortion and rotation, the effects of which become more substantial with smaller A-site cations [44]. This enhances the electrical resistance, which affects the total catalytic activity for oxygen reduction [45–47]. According to Sunarso et al. [48], Cobalt (Co)-based perovskites have the highest current density and the best onset potential for reducing oxygen. BT is a useful room temperature ferroelectric material with high dielectric constant, pyroelectric and piezoelectric capabilities, low dielectric loss, chemical stability, and minimal toxicity [49]. The incorporation of Nickel into BT samples increases the dielectric permittivity of substances more than using an undoped specimen would, as suggested by Jana et al. [50]. Mn can greatly lower dielectric loss while raising the dielectric constant [51]. Ferromagnetic ordering has been demonstrated in BT compounds with Fe, Mn, Ni, and Co doping [52–54]. The addition of a multivalent 3d transition metal ion can make $BaTiO_3$ magnetic, making it a potential multiferroic material [37,55,56]. Barium atoms in $BaTiO_3$′s perovskite structure can be easily replaced by 3d transition metals, primarily due to their similarities in size and valence [57]. This allows for substitution or co-substitution at the A site with mono-, di-, or trivalent cations or the B site with di-, tri-, tetra-, or pentavalent cations.

The barium site in ceramics known as BCT ceramics is substituted in this study using various amounts of cobalt concentrations. Examining how the substitution of Co influences the structural and optical phase transitional properties of $BaTiO_3$ (BT) is the main goal of this work. This will be done by producing a wide range of $Ba_{1-x}Co_xTiO_3$ (x = 0, . . . , 1) (BCT) materials. Various spectroscopic and microscopic perspectives will be used to completely

explain these perovskite materials. The objective is to evaluate the effects of both structure and composition while achieving the perfect balance through catalytic activity.

2. Materials and Methods

2.1. Starting Reagents

The destabilization of colloidal solution (DCS) technique was used to successfully synthesize $BaTiO_3$ crystals with Cobalt Co^{2+} (BCT) substitutions [58,59]. This method offers excellent stoichiometry control and good powder homogeneity despite crystallization occurring at a relatively low temperature [60]. The precursors used in the process include high purity barium nitrate [$Ba(NO_3)_2$] (99.8% purity, Alfa Aesar), TiO_2 from Sigma-Aldrich (99.98% purity, Ants Ceramics), nitric acid ([HNO_3] > 70%), and cobalt (II) chloride hexahydrate ([$CoCl_2 \cdot H_2O$] (99.9% purity, purchased from Sigma-Aldrich, Saint-Quentin Fallavier, France)). Ethylene glycol anhydrous ([$HOCH_2CH_2OH$] (pro-analyst grade with purity more than 95%)) and distilled water were used as the solvents.

2.2. Experimental Process

A novel sol–gel-assisted solid-phase method for synthesizing nano BT ceramics at high temperatures is described in [61]. The authors demonstrate how the synthesis process affects the performance of the photocatalytic process and the conversion of the tetragonal phase in this study [61]. For that, a typical experiment entailed mixing barium nitrate and cobalt (II) chloride hexahydrate in 60 mL of deionized water with magnetic stirring in the appropriate weighted proportions based on the molar ratio of Ba/Co. In addition, a molar proportion of TiO_2 was dissolved in pure nitric acid while being vigorously stirred using a thermo-magnetic stirrer at 50 °C for two hours to achieve total dispersion and the formation of the intermediate agent [$Ti(NO_3)_4$].

The solution containing barium nitrate, cobalt chloride hexahydrate, and dispersed TiO_2 in nitric acid was further treated with 5 mL of ethylene glycol anhydrous to prevent particle agglomeration and facilitate dispersion. The resulting mixture was then stirred at 50 °C for 4 h to form a colloidal gel, which was dried at 100 °C for 12 h. The dried gel was then heated at a rate of 5 °C/min to 1000 °C for 3 h in a muffle oven. The particle size homogeneity of the BCT compound was verified prior to sample removal by allowing the reaction mixture to air-cool to room temperature. Figure S1 shows a flow diagram of the various steps involved in the sample preparation process.

2.3. Characterization Methods

2.3.1. PXRD Analysis

The crystal structure and the phase purity of all samples were determined by powder X-ray diffraction (PXRD) analysis. PXRD patterns were obtained using a Bruker D8 Advance instrument with Cu-Kα radiation and a step interval of 0.02 degrees.

The Diffrac Plus software was utilized to identify the material-phase based on the PXRD measurements. Rietveld refinement was used to quantitatively analyze the structural characteristics from the PXRD patterns using the PROFEX BGMN refinement program [62].

2.3.2. TEM Scanning and Energy-Dispersive X-ray Spectroscopy (EDX)

Transmission electron microscopy (TEM) using a FET Tecnai G2 operating at 200 kV revealed the nanostructure and morphology of powdered materials. TEM specimens were prepared by breaking the samples while submerging them in ethanol. A drop of the suspension was then deposited onto a copper grid-supported holey carbon film. Local chemical analysis was performed using an energy-dispersive X-ray spectroscopy (EDX) system coupled with a Carl Zeiss Ultra 55 field-emission scanning electron microscope.

2.3.3. Fourier Transform Infrared Spectroscopy (FTIR)

The Fourier transform infrared spectra (FT-IR) were measured using a Bruker VERTEX 80V spectrometer, which was configured in the spectral range of 4000 to 400 cm^{-1}

(corresponding to terahertz frequencies of 1016 Hz to ultraviolet frequencies of 1012 Hz) at a temperature of 25 °C. The optical resolution of the instrument was <0.06 cm^{-1}.

2.3.4. Photoluminescence Spectroscopy (PL)

To investigate the optical properties of semiconductors, PL spectra were measured over a spectral range of 300 to 500 nm using two different excitation wavelengths. The measurements were conducted by varying the temperature of the sample between 10 and 450 Kelvin, using a closed-circuit helium cryostat, and two excitation lasers with wavelengths of 266 nm and 447 nm. The RF-5301 PC spectrophotometer equipped with a 290 nm filter was used for the measurements.

2.3.5. UV-Visible Spectroscopy

The UV-visible diffuse reflectance and absorbance spectra of all samples were recorded using a Shimadzu UV-2600 spectrophotometer in the spectral range from 200 to 400 nm.

2.3.6. Photocatalytic Application

Metal/halide-perovskites have gained interest for their potential as photocatalysts due to their adjustable preparation and the ability to alter their bandgap by modulating the ratio of halides and metals. These compounds are intriguing options for photocatalytic applications, according to Schanze Kirk et al. [63]. The photocatalytic activity of the produce BCT samples was evaluated in this study by degrading 10 ppm of Cibacron Brilliant Yellow 3G-P (Y) solution in a cylindrical quartz glass reactor with an effective vessel volume of 80 mL.

Cibacron Brilliant Yellow 3G-P($C_{25}H_{15}Cl_3N_9Na_3O_{10}S_3$) was obtained from Sigma-Aldrich, a division of Merck KGaA, Darmstadt, Germany. The molecule has three sulfonate groups (Figure S2), which are negatively charged in aqueous solution. It has a molecular weight of 831.02 g mol^{-1}, a color index number of 18,972, and a maximum absorption wavelength of 404 nm [64]. Double distilled water was used for all experiments, and nitric acid (purchased from TEDIA, supplier of high-purity solvents and acids, located in Fairfield, USA) and sodium hydroxide (Sigma-Aldrich, a division of Merck KGaA, Darmstadt, Germany) were used to adjust the pH to 5. The dye was used without further purification, and all other chemicals used were of analytical grade unless otherwise stated [65].

The experimental setup involved a 230 V~50–60 Hz, 2066 W UV lamp with a cooling water circuit, which served as a side light source, emitting light at wavelengths of 365 nm and 254 nm. The distance between the photoreactor and the UV lamp was 6.0 cm. A suspension of BCT photocatalysts (at a concentration of 66 ppm) in 50 mL of solution (denoted as Y) was stirred in the dark for 30 min to achieve adsorption–desorption equilibrium before the photocatalytic reaction. After that, the suspension was continuously exposed to UV radiation for 180 min at 25 °C while being aerated with air flowing via a mini-pump at a flow rate of 4.2 L/min. At various time intervals, a sample of the suspension was taken out and centrifuged for 10 min to obtain clear solution of (Y), which was then analyzed for its concentration using a Shimadzu UV-2600 spectrophotometer at 254 nm. The residual rate of (Y) can be calculated using a specific equation [66]:

$$D(\%) = \frac{A_t}{A_0} \times 100, \quad (1)$$

where A_0 is the initial concentration of (Y), A_t is the concentration of (Y) after reacting t minutes.

Table 1 (below) provides an overview of multiple researches investigating the use of photocatalysts to remove different organic pollutants, with a specific focus on the BT catalyst. Table 2 organizes and presents these research findings.

Table 1. Overview of various photocatalysts for CBY 3G-P degradation.

Catalysts	Irradiation Source	Rate (%)	Time (min)	References
Nanosized ZnO	Simulated solar light	98	60	[67]
γ-Fe_2O_3	Visible light	68	120	[68]
Ball milled TiO_2	UV-Visible	78.1	120	[69]
Core/Shell Fe_3O_4@Al_2O_3-PMo	UV light	>90	300	[70]
Degussa P25	UV-A	71.3	111	[43]
Ag-ZnO	Visible light	65	120	[71]
Brazilian peats (DP) and (FP)	UV-Visible	95.56	270	[72]
Amourphous $Fe_{78}Si_9B_{13}$ and $Fe_{73.5}Si_{13.5}B_9Cu_1Nb_3$	Visible light	100 70	5 20	[73]
Nano-articulate crystals	Sun light	94	180	[74]
TiO_2 semi-conductor	UV-Visible	95	120	[75]

Table 2. Summary of metal-doped $BaTiO_3$ photocatalysts applied to the degradation of organic pollutants.

$BaTiO_3$ Doped Materials	Dye	Irradiation Source	Degradation Rate (%)	Time (min)	References
Fe^{3+}-doped BT	Methyl orange (MO)	Sun light	70	90	[76]
Ce-doped BT	Methylene blue (MB) Methylene violet (MV) (CR)	UV-Vsible	90.2 82.4 78.5	120	[77]
Cr-doped BT	Nitrobenzene Aniline yield	Microwave	99.9 99.7	180 180	[78]
Fe-, Co-, Ni-doped BT	Azoxybenzene Nitrobenzene	*	93, 84 (Fe) 91, 80 (Ni) 100, 93(Co)	*	[79]
Sr-doped BT	Rhodamine B (RhB)	Dark condition	98	*	[80]

* Unidentified.

3. Results and Discussion

3.1. Study of Structurals

3.1.1. Qualitative PXRD Analysis

Good crystallinity is an essential property of nanoparticles as it influences their stability, reactivity, and overall performance in a variety of applications. The pure BT nanoparticle powder, in this case, appears to have a high crystallinity degree, which could make it suitable for a variety of applications, according to the results of the PXRD study. Figure S3 displays the PXRD pattern of the BT nanoparticle powder as it was formed. The PXRD data displays distinctive reflections, demonstrating that the particles have an extremely ordered atomic structure. The findings suggest that BT nanoparticles crystallize exclusively in the perovskite phase without passing through any further phases. According to JCPDS files, the appropriate planes for indexing reflections are (hkl). The primary peaks in the PXRD pattern located at 2θ°: {22.09, 22.15, 31.49, 31.52, 38.86, 39.01, 45.21, 45.32, 50.87, 50.96, 56.14, 56.21, 65.76, 65.80, 70.38, 74.84, 79.23, 79.42, 83.51, 83.74, 91.94} are identified as belonging to the tetragonal phase planes of the perovskite structure of the powdered BT nanoparticles, and they are found to be in good agreement with the values of JCPDS files no. 75-2121.

Additionally, in the case of BCT samples, nanoparticles are formed, which are discernible in all concentration ranges (variable Cobalt substitution) (Figure 1). The presence of sharp (002)-(200) doublet peaks at 45.21–45.32 (°2θ) and a single (111) peak at 2θ~38.86° to

39.01° supports this finding, as shown by Mahmoud et al. [81]. Table 3 also shows that the PXRD data of the BCT ceramics exhibit a transitional structure for ($x \geq 0.3$). This indicates that the perovskite structure of BT nanoparticles was maintained and that Co^{2+} ions were typically absorbed into the lattice for low bulk density ($x = 0.3$). Furthermore, it shows that adding more Co ions to BT might possibly replace Ba, raising the 45.21° characteristic peak to lower 2θ° values, and that no secondary phases result from Co substitution in the BT lattice in this domain. Carrying on this study of phase's identification, a scan match was performed via comparison with standard JCPDS PDF data base structures files reported in the literature that indicate the presence of intermediary phases for the formation of $x \geq 0.3$, as labeled in Figure 1.

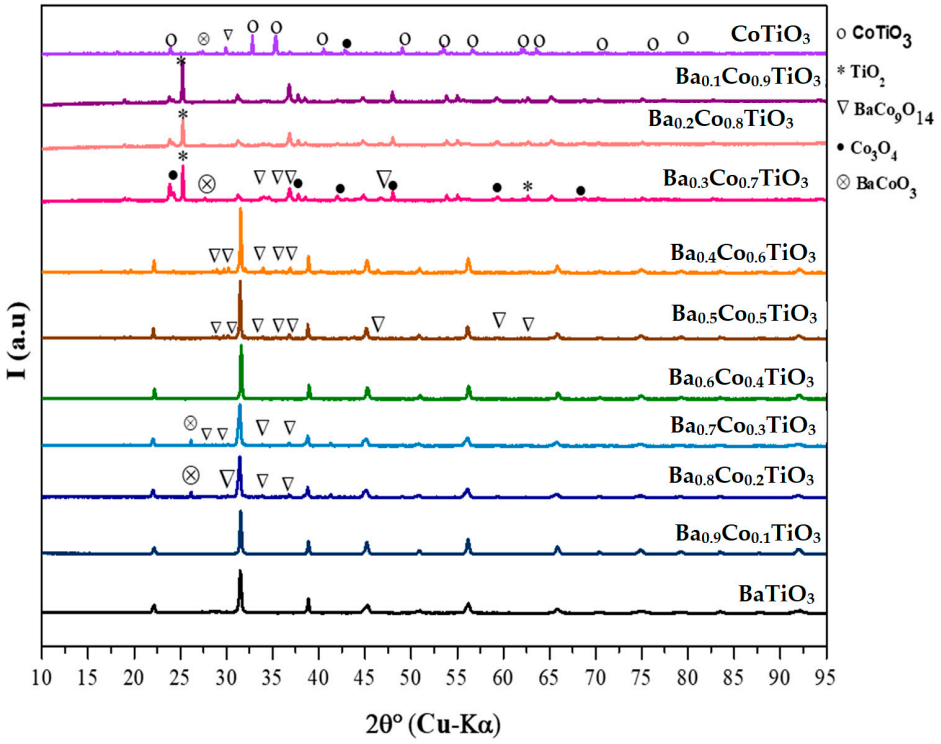

Figure 1. Characteristic parts of PXRD patterns of $Ba_{(1-x)}Co_xTiO_3$ ($x = \{0, \ldots, 1\}$) Ba/Co-substituted barium titanate.

Table 3. Crystallographic data of synthesized $Ba_{(1-x)}Co_xTiO_3$ specimens.

Compound	Position (°2θ)	d_{hkl} (nm)	Crystallite Size (nm)	Crystal System	Identification Reference
$BaTiO_3$	31.49	0.284	114	Tetragonal	01-075-2121
$Ba_{0.9}Co_{0.1}TiO_3$	31.52	0.283	97	Tetragonal	01-079-2264
$Ba_{0.8}Co_{0.2}TiO_3$	31.58	0.283	94	Tetragonal	01-079-2265
$Ba_{0.7}Co_{0.3}TiO_3$	31.43	0.284	9388	Hexagonal	00-008-0372
$Ba_{0.6}Co_{0.4}TiO_3$	31.47	0.284	87,119	Hexagonal	00-051-1873
$Ba_{0.5}Co_{0.5}TiO_3$	31.46	0.284	104	Hexagonal	00-051-1873
$Ba_{0.4}Co_{0.6}TiO_3$	31.52	0.283	10,496	Hexagonal	00-051-1873
$Ba_{0.3}Co_{0.7}TiO_3$	25.27	0.352	66,137	Hexagonal	00-051-1873
$Ba_{0.2}Co_{0.8}TiO_3$	25.27	0.352	69,118	Rhombohedral	00-001-1040
$Ba_{0.1}Co_{0.9}TiO_3$	25.24	0.352	78,134	Rhombohedral	01-077-0153
$CoTiO_3$	32.79	0.273	56	Rhombohedral	01-077-1373

Nevertheless, the system maintains the perovskite structure of $BaTiO_3$ at a small amount of Ba substitution. As the level of Ba substitution is increased, the crystal structure transforms into the $CoTiO_3$ ilmenite structure. In the $BaTiO_3$-$CoTiO_3$ system, the phenomena of intermediate phases emerging during the phase transition from perovskite $BaTiO_3$ to ilmenite $CoTiO_3$ is well-known. The crystal structure of the material changes from perovskite to ilmenite as the Ba substitution level rises [82–85]. However, this change does not occur instantaneously. In fact, this transition must occur through the emergence of intermediary phases in which perovskite and ilmenite coexist [86].

An inability to accomplish a direct transformation between the two crystal forms results in the creation of intermediate phases. Since $BaTiO_3$ and $CoTiO_3$ have differing lattice properties and crystal symmetries, switching between these two crystal forms causes a substantial alteration in the material's atomic composition. The challenging nature of this transformation leads to the emergence of intermediary phases. The creation of intermediate phases is a natural byproduct of the gradual change from the perovskite to the ilmenite structure. The composition and characteristics of these intermediary phases can change depending on the synthesis conditions, such as temperature, pressure, and annealing time.

As a result, the presence of these intermediary phases, which are expected to be part of the phase transition process, is responsible for the impurities emerging in the samples at higher Ba levels of substitution. It is significant to consider that the development of intermediate phases in the $BaTiO_3$-$CoTiO_3$ system results from the complicated nature of the phase transition between the perovskite and ilmenite structures, not necessarily from poor sample quality.

The average particle size was calculated using the classical Scherer formula [87]:

$$d = k\lambda/\beta\cos\theta, \quad (2)$$

In the Sherrer formula, "d" represents the average crystallite size, "k" is the shape factor equal to 0.9, "λ" is the wavelength of the X-rays used (λ = 1.5406 Å), "β" is the FWHM of the characteristic peak, and "θ" is Bragg's diffraction angle. This formula only considers the influence of crystallite size on the PXRD peak broadening. The results presented in Table 3 indicate that all of the obtained crystallite sizes fall within the range of 56–114 nm, suggesting that an increase in cobalt concentration is accompanied by a decrease in particle size. Additionally, a series of phase transitions are exhibited by the $BaTiO_3$-$CoTiO_3$ system as the Ba substitution level is increased.

With a rise in Co concentration in the solid solution, the unit cell of BCT samples tends to decrease. Examining the cobalt ions in the BCT unit cell could provide insight into this phenomenon. In our case, Co ions with a coordination number of 12 are situated in the A sub-lattice, occupying the Ba site. According to [88], the difference in ion radii between Ba and Co ions refers to the saturation and phase transition processes.

3.1.2. Quantitative PXRD Analysis

The BCT sample underwent Rietveld refinement using PROFEX BGMN software to perform quantitative PXRD analysis. Figures 2 and S4a–j show the BCT's refined PXRD data. The refinement supports the PXRD data analysis findings and confirms the transition from a tetragonal single phase to a rhombohedral phase for all increasing Co specimens. This transition was observed through Rietveld PXRD fitting profiles, as reported by Wang et al. [89], which revealed a typical tetragonal structure with P4mm (99) space group. Table 4 lists the different structural characteristics identified through the refinement of the BCT PXRD data.

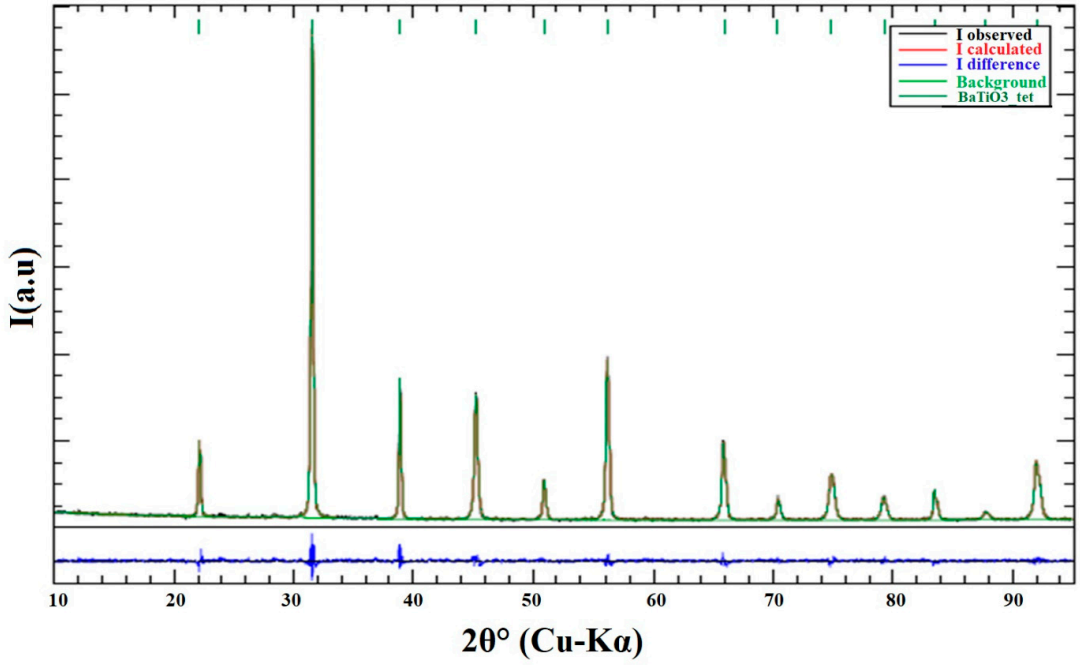

Figure 2. Results of Rietveld refinement of $BaTiO_3$ structures. Short vertical bars indicate the positions of diffraction maxima in the major tetragonal phase.

Table 4. Rietveld refinement structural parameters and unit cell data for BT and BCT NPs.

Compound $Ba_x Co_{1-x} TiO_3$ x = {0, . . . , 1}	Unit Cell						Reliability Factors			Space Group
	a (Å)	b (Å)	c (Å)	α (°)	β (°)	γ (°)	R_P	R_{WP}	GoF	
$BaTiO_3$	3.9886	3.9886	4.00060	90.00	90.00	90.00	5.57	06.99	1.25	P4mm
$Ba_{0.9}$ $Co_{0.1}TiO_3$	3.9980	3.9980	4.01800	90.00	90.00	90.00	5.62	11.11	1,97	P4mm
$Ba_{0.8}Co_{0.2}TiO_3$	3.9980	3.9980	4.02200	90.00	90.00	90.00	5.29	14.72	2.78	P4mm
$Ba_{0.7}Co_{0.3}TiO_3$	3.9900	3.9900	12.2114	90.00	90.00	120.0	3.53	16.46	4.66	P63/mmc
$Ba_{0.6}Co_{0.4}TiO_3$	3.6983	3.6983	12.6023	90.00	90.00	120.0	3.50	6.40	4.60	P63/mmc
$Ba_{0.5}Co_{0.5}TiO_3$	2.7240	2.7240	11.9640	90.00	90.00	120.0	5.70	10.87	1.32	P63/mmc
$Ba_{0.4}Co_{0.6}TiO_3$	2.9301	2.9301	11.9980	90.00	90.00	120.0	2.83	09.98	3.52	R-3
$Ba_{0.3}Co_{0.7}TiO_3$	5.4860	5.4860	7.03200	90.00	90.00	120.0	1.78	04.74	2.66	R-3
$Ba_{0.2}Co_{0.8}TiO_3$	5.4860	5.4860	7.03200	90.00	90.00	120.0	1.78	05.29	2.97	R-3
$Ba_{0.1}Co_{0.9}TiO_3$	5.0760	5.0760	5.48600	54.83	54.83	54.83	1.53	04.87	3.18	R-3
$CoTiO_3$	5.0760	5.0760	5.48600	54.83	54.83	54.83	1.78	04.74	2.66	R-3

Bragg reflections and variations between the experimentally measured patterns and predicted patterns of selected samples were obtained at room temperature. The samples were identified as being single-phase crystalline and chemically pure based on the findings of the Rietveld investigation of PXRD. The structures of all samples were carefully refined, and the results are quite interesting. The unsubstituted and low-substituted samples, limited by x = 0.3, exhibited a single crystal phase, and Rietveld refinement resulted in a tetragonal structure with P4mm space group. The highest substitution sample (x = 1) crystallized in a rhombohedral phase with R-3 space group, as a result of an increasing Co substitution rate, which caused a structural phase transition. For pure BT, the goodness of fit (GOF) was found to be approximately 1.25, while the BCT sample series exhibited a reasonably good fit.

The effect of Co^{2+} content on the lattice parameters (a, c) was estimated from fitting PXRD data, as well as the decrease in tetragonality (c/a) with increasing Co^{2+} ratio. The

variations in the lattice parameters are due to the incorporation of Co^{2+}/Ba^{2+} into the lattice. Taking the ionic radius into account, it is believed that Co^{2+} (with a radius between 0.58 and 0.90 Å) has a relatively small ionic radius compared to Ba^{2+} (with a radius of 1.35 Å). This difference induces a lattice strain, according to Mahmoud et al. [90], and significantly causes the shrinkage of the optical bandgap, as manifested by absorption red shifting in the UV spectra.

3.1.3. FT-IR

The FT-IR spectra of BCT and pure BT are shown in Figure 3. The presence of barium titanate is indicated by the bond at 1440 cm^{-1}, which is the vibration of the Ba-Ti-O bond. The band observed in the 3440–2750 cm^{-1} range represents O-H vibrations. The band near 1635 cm^{-1} may be caused by water in the samples, which is attributed to the H-O-H bending vibration mode. The band around 525 cm^{-1} is assigned to O-Co-O bond bridging vibration, and the band close to 647 cm^{-1} is assigned to Co-O stretching. The two broad characteristic bands at 850 and 520 cm^{-1} represent the Ti-O vibration modes and indicate the disappearance of the alkoxide groups. These bands are assigned to the stretching vibrations of $[TiO_6]_2$-octahedron (Table 5) [91]. Therefore, the obtained results are in good agreement with those of the X-ray diffraction analysis.

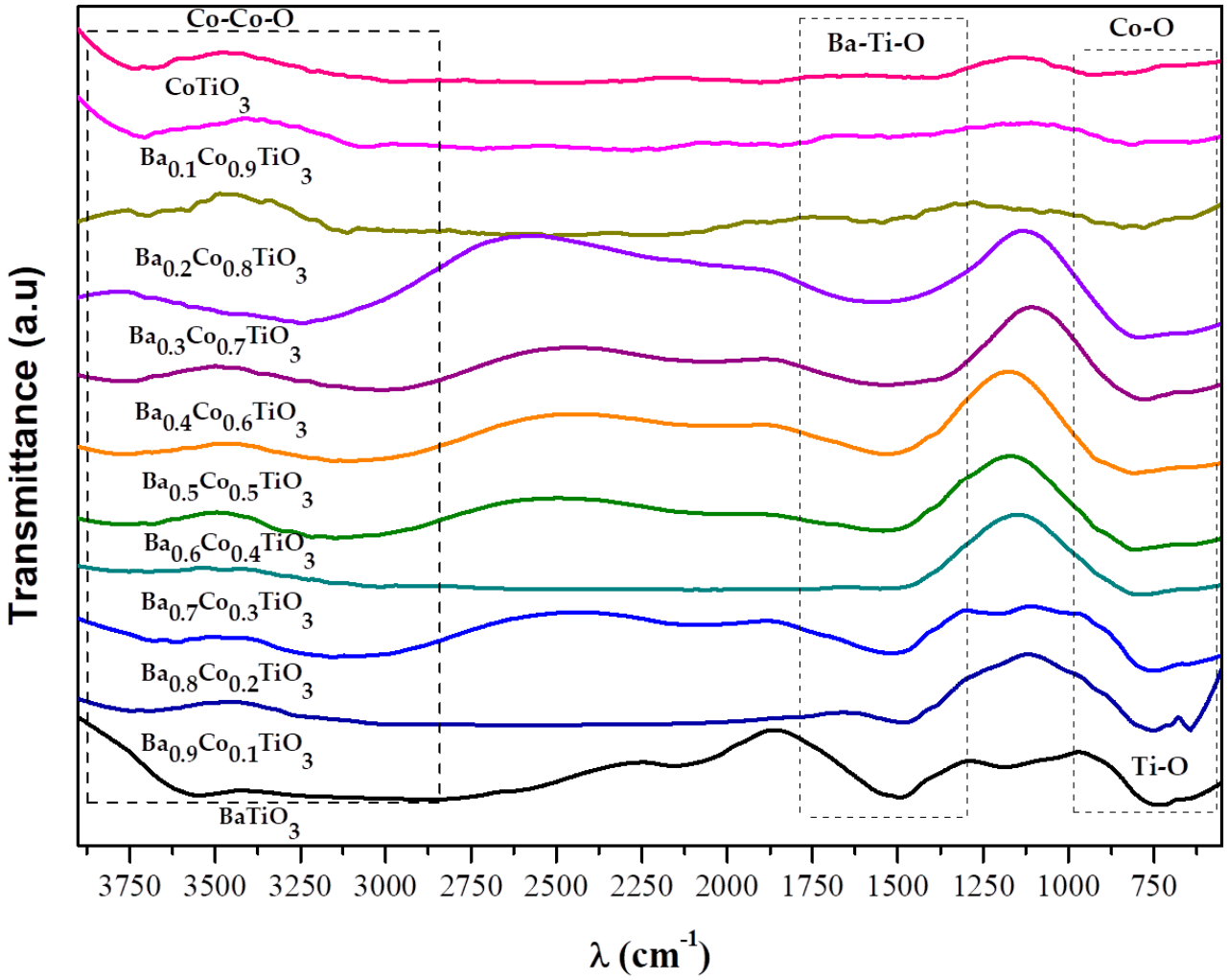

Figure 3. FTIR spectra of Ba/Co-substituted barium titanate samples.

Table 5. Peak positions and assignment of infrared spectra of investigated various barium cobalt titanate nanoparticles.

Bandes (cm^{-1})	Liaisons	Modes
1631 and 1440	Ba-Ti-O	Elongation
520, 545 and 850	Ti-O	Elongation
525	Co-O	Elongation
647	O-Co-O	Elongation

3.1.4. TEM and EDX

Figure 4a reports the surface structure and chemical composition of the $Ba_{0.4}Co_{0.6}TiO_3$ sample (x = 0.6) at the nanoscale. This obviously quasi-hexagonal shape is attributable to the phase transition to the R-3 space group. Additionally, the sample's microstructure and grain arrangement are successfully represented. Other samples with a particular x value, selected using a common method, highlight observed phase transitions and are shown in supplementary Figure S5. Indeed:

- Figure S5a,b show TEM images for pure BT powder, which were composed of irregular cubic-shaped solids with interplanar spacing d_{hkl} equal to 0.32 nm and a size range between 30 and 114 nm, appearing as several micron-sized solids. Additionally, the highly crystalline surface textures and lack of agglomeration, along with the grain's tendency to grow uniformly, are visible.
- Figure S5c,d depicts TEM images of the $Ba_{0.8}Co_{0.2}TiO_3$ nano-compound, which had clearly defined quasi-cubic forms, sharp grain boundaries, and little agglomeration. The d-spacing was approximately 0.24 nm.
- Figure S5e,f show TEM images of the $Ba_{0.6}Co_{0.4}TiO_3$ sample, where a secondary spherical shape with a size range between 34.41 nm and 54.10 nm emerges into the lattice and is attributed to an intermediate produced phase in agreement with the results of Rietveld analysis. Additionally, we can clearly see a hexagonal shape, attributable to phase transition of the P63/mmc space group.
- Figure S5g,h displays TEM images of $Ba_{0.2}Co_{0.8}TiO_3$ with a range of sizes between 78.63 nm and 99.79 nm and a high-resolution treatment under 5 nm of scale; the d-spacing was measured for being 0.14 nm.
- The $CoTiO_3$ single phase (full cobalt substitution rate) TEM images in Figure S5i,l have the fewest spherical-shaped agglomerations. The average particle size of the CT nanoparticles ranged from 36 to 93 nm, with a constrained size distribution.

These results validate the PXRD studies and demonstrate the existence of a tetragonal phase transition up to x = 0.3 value. Furthermore, TEM images of the BCT complex series reveal that cobalt substitution in the BT lattice has a major impact on the grain size and shape of the samples. However, this effect diminishes with the increasing cobalt ratio in the nanopowder.

It is important to note that the samples' composition was confirmed, and the microstructure and grain arrangement were also considered. To test the composition and elemental integrity of the pure BT and $Ba_{0.4}Co_{0.6}TiO_3$ sample we used energy dispersive analysis of X-rays (EDX)—the most trustworthy method. The energy dispersive spectra (EDX) of the BT and BCT for x = 0.6 are shown in Figure 4b,c, respectively. Figure 4b shows that every element is present in the sample, and no necessary element has been left out. No extraneous spectral component is also discernible. The composition and concentration of the components also affect the intensity strength of the visible peaks.

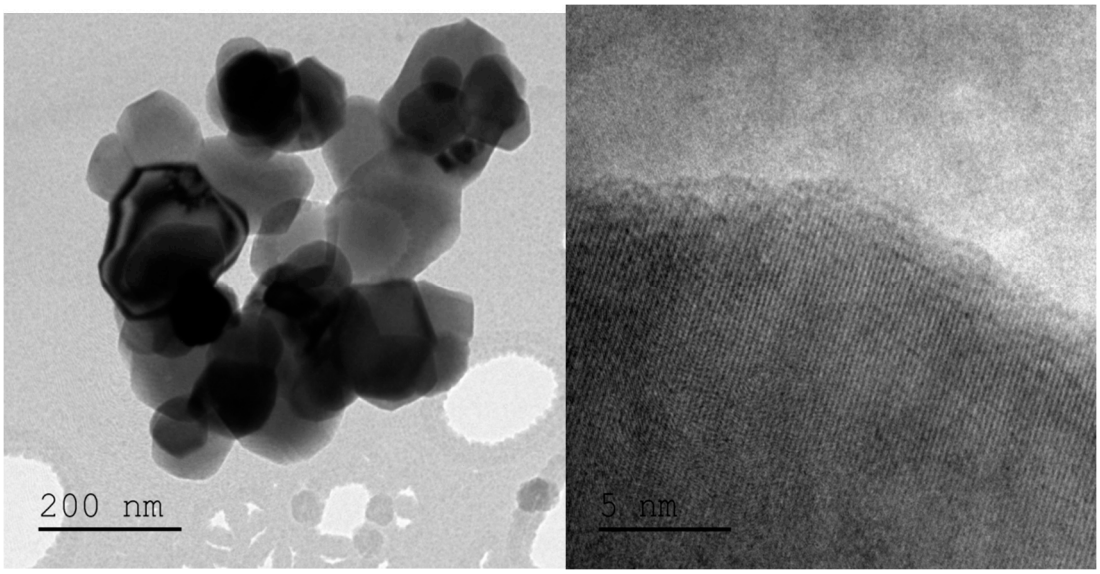

(**a**)

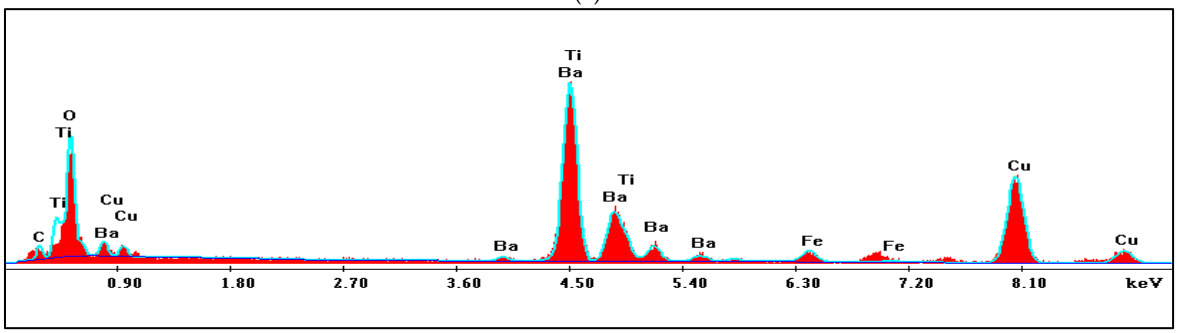

(**b**)

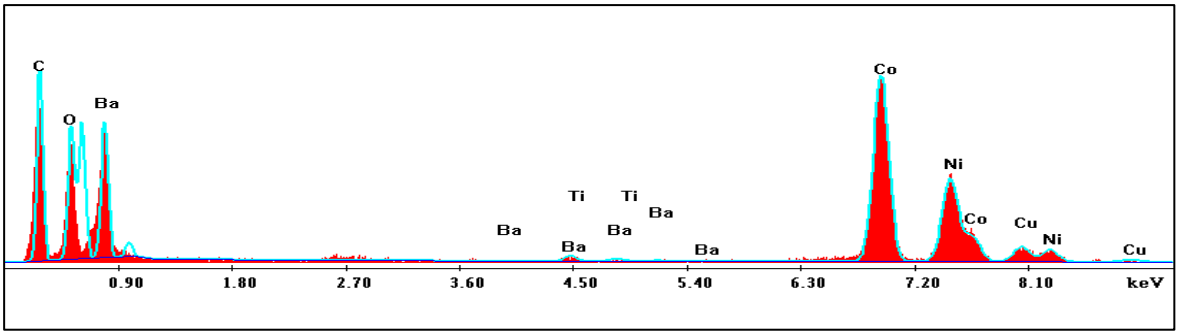

(**c**)

Figure 4. (**a**) TEM micrographs and high-resolution images for $Ba_{1-x}Co_xTiO_3$ sample with (x = 0.6). EDX spectrum of: (**b**) pure BT and (**c**) $Ba_{0.4}Co_{0.6}TiO_3$ (x = 0.6) nano-heterostructure.

By using elemental energy dispersive spectroscopy, the distribution of the barium, cobalt, and oxygen elements was appropriately described. The EDX findings also showed the presence of titanium, proving that BT nanoparticles were successfully formed and disclosing the substituted and host components of the samples. As a result, the purity and stoichiometry of BT can be deduced, as well as the spectra for BCT compounds (Figure 4c) with x = 0.6, representing the distribution of the various elements present in the spectroscopic localization space in this sample. The absence of a signal for Ti in the BCT (x = 0.6) sample could be attributed to several purposes, such as the amount of Ti present, its position within the surface's heterogeneous distribution, or EDX equipment limitations. For such, there is quantitative information in Table 6 (below) that displays the

atomic/weight percentage for various elements. According to TEM data that are roughly identical to those from XRD, the BCT series was able to grow utilizing the sol–gel method.

Table 6. Atomic/weight percentage for $Ba_{0.4}Co_{0.6}TiO_3$.

Element for (x = 0.6)	Weight %	Atomic %
Ba (L)	7.1	3.2
Ti (K)	0.2	0.3
Co (K)	92.7	96.6
Total	100.0	100.0

3.2. Optical Studies

3.2.1. UV-Visible

After confirming the acquired structure and phase developed in the selected studies, the required characteristics were analyzed. Optical features of the synthesized complexes are summarized in Figure 5. Figure 5a shows the UV-visible absorption spectra of $Ba_{1-x}Co_xTiO_3$ samples in the wavelength range of 200–400 nm. The absorption curves of BCT exhibit a red-shift compared to those of pure BT, which is attributed to the significant absorption band of cobalt ions in the 200–250 nm range. These spectral characteristics quantitatively demonstrate that increasing the cobalt content results in increased optical absorption in a manner that is consistent with the findings of Kutapan et al. [92], with a distinct wide band of absorption edge observed in the wavelength range between 270 and 300 nm.

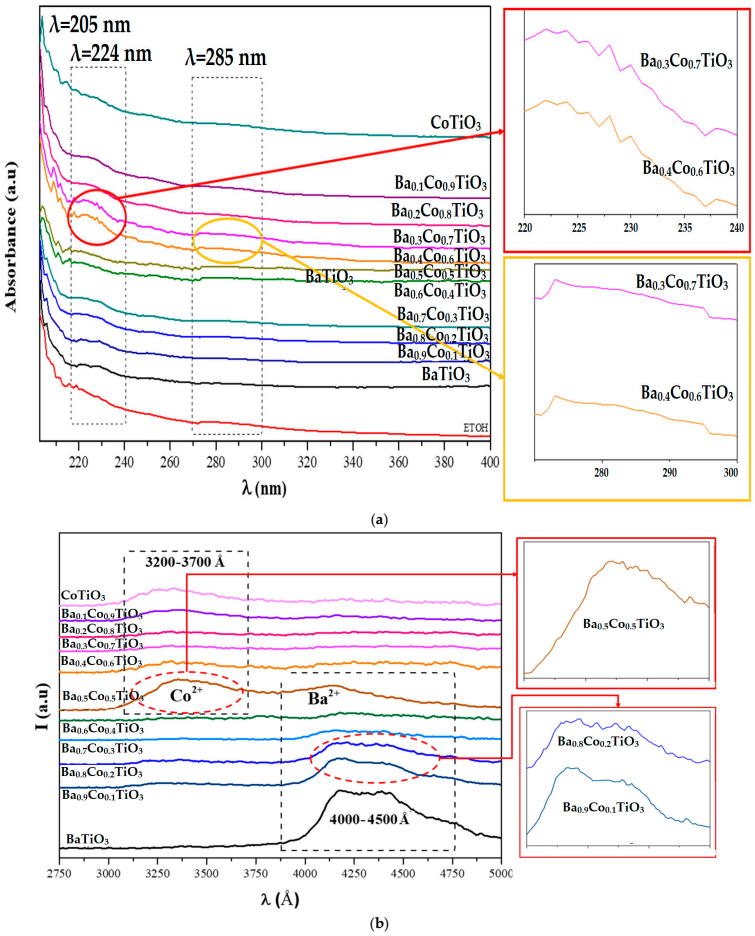

Figure 5. (**a**) UV-Vis absorption spectral of synthesized BCT nanoparticles (**b**) Photoluminescence spectra of all BCT nanoparticles.

To determine the optical bandgap, which is a crucial factor in evaluating the performance of electronic devices, we used the Kubelka–Munk function with the Tauc Plot method [93,94] to convert the diffuse reflectance spectra (DRS) into the absorbance coefficient. The Kubelka–Munk $[F(R)h\nu]^n$ function was used to generate a graph, with the y-axis representing the function value and the x-axis representing the energy ($E = h\nu$) of the absorbed light. To measure the allowed bandgap directly, the power "n" is set to 2.

To estimate the bandgap, the extrapolated line is used to intersect the plot's energy axis. The curve is extrapolated at the point where it displays a sharp edge. This intercept represents the value of the energy bandgap for the sample. For the $Ba_{1-x}Co_xTiO_3$ (x = 0.6) sample, we found the intercept value to be 3 eV, as shown in Figure 6a. The bandgap values of all samples {x = 0, . . . , 1}, estimated with the same method (Figure S6) and presented in Table 7, were consistent with previous reports demonstrating the decrease in the direct band gap value as a function of the cobalt substation rate (Figure 6b). It is worth noting that the bandgap value can decrease to $E_G = 2.95$ [95] due to several factors, including the merging of parent and impurity bands, electronic interactions, scattering by impurities, and lattice compression. These factors contribute to the shrinking of the optical bandgap value, leading to a lesser forbidden band, which is in line with our previous structural studies.

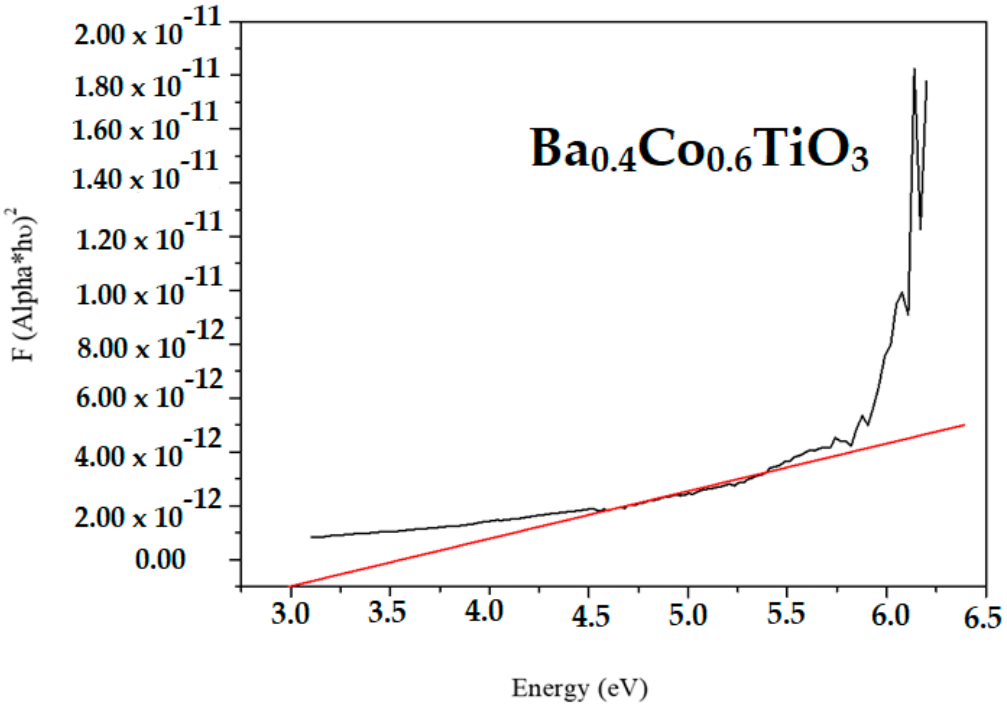

(**a**)

Figure 6. *Cont.*

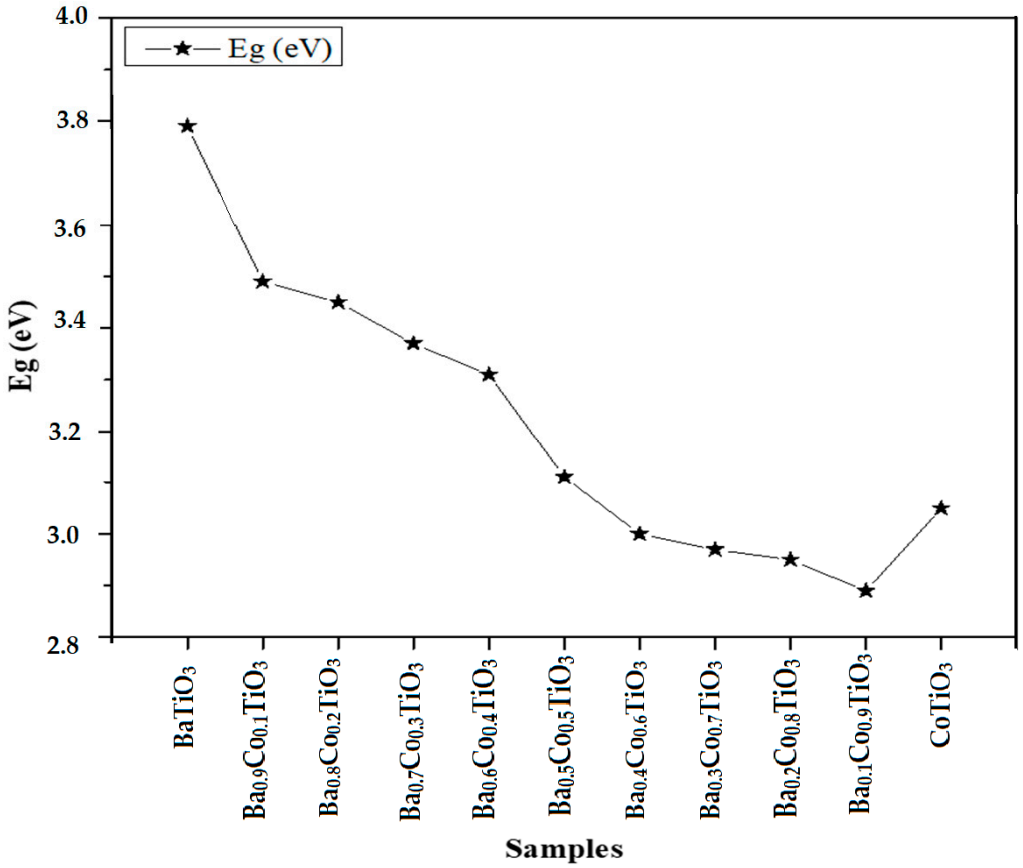

(**b**)

Figure 6. (**a**) UV-Vis DRS spectra of $Ba_{0.4}Co_{0.6}TiO_3$ solid material for optical band-gap determination and (**b**) variation of the gap energy as a function of the cobalt substitution rate.

Table 7. Calculated band gap by the Tauc Plot method for all of the nano-compounds.

Compounds	Band Gap (eV)
BaTiO3	3.79
Ba0.9Co0.1TiO3	3.49
Ba0.8Co0.2TiO3	3.45
Ba0.7Co0.3TiO3	3.37
Ba0.6Co0.4TiO3	3.31
Ba0.5Co0.5TiO3	3.11
Ba0.4Co0.6TiO3	3.00
Ba0.3Co0.7TiO3	2.97
Ba0.2Co0.8TiO3	2.96
Ba0.1Co0.9TiO3	2.95
CoTiO3	3.05

3.2.2. PL

Over a temperature range of 10 to 450 Kelvin, the samples were examined using a He fluorescence spectrometer. Two excitation sources, with wavelengths of 266 nm and 447 nm, were used to excite the samples. The characterization and improvement of materials for photocatalytic applications can benefit from information obtained from photoluminescence

spectroscopy. The bandgap of the material can be determined by looking at the peak position in the photoluminescence spectrum, which is crucial for finding out its electrical structure and optical characteristics.

The analysis of the emission at the violet region between 400 and 450 nm is shown in Table 8. For all curves of $Ba_{1-x}Co_xTiO_3$, {x = 0, . . . , 0.4}, the emission was observed to be sharp, and the cobalt-barium substitution resulted in a reduction in the emission intensity. Figure 5b illustrates how point defects, such as vacancies and complexes with barium interstitials, affect the visible emission. For samples with x values ranging from 0.5 to 1, the emission spectra were examined as well at a second excitation wavelength of 340 nm. This excitation wavelength corresponds to a defect emission that can occur via several different routes involving a variety of states inside the allowed band gap. This suggests that PL and the localized states within the band gap are tightly connected. With an excitation wavelength of 447 nm and an emission peak centered around 340 nm, the sample with x = 0.6 showed both emission peaks at 340 nm and 430 nm. This implies that both values are lower than the band gaps for these samples according to the findings observable in [96]. Understanding a material's photocatalytic performance requires knowledge about the creation and recombination of charge carriers, which photoluminescence can provide. It is widely recognized that the probability of electrical transitions between the valence and conduction bands, which lead to PL emission, is increased by the presence of localized states within the band gap. The violet emission detected in the $Ba_{1-x}Co_xTiO_3$ samples is attributed to surface-localized states and a photogenerated hole recombining with a single ionized charged state. The PL emission intensity is greatly influenced by the interaction between the sample and the excitation wavelength. Adding more cobalt seemingly reduces the luminescence of the 430 nm peak, which is connected to the disappearance of barium anion vacancies. Prior research [97] has shown that PL emission in semiconductors occurs via a variety of paths involving a variety of states inside the forbidden band gap. PL emission is intimately tied to localized states within the band gap. In the case of $Ba_{1-x}Co_xTiO_3$ samples, the valence band is made up of oxygen 2p states, while the conduction band is made up of barium s, titanium s, and d states. The band gap may become populated with delocalized electronic states as a result of electron transport between the barium and titanium ions. The production of clusters (such as TiO_2 or TiO_5) in samples with x values of 0.5 to 1 is thought to be responsible for the occurrence of s and p states inside the band gap energy.

Table 8. Photoluminescence emission bands colors of $Ba_{1-x}Co_xTiO_3$ NPs.

Compound	Emission Peaks Wavelength (nm)	Ray Emission Color Range
$BaTiO_3$ $Ba_{0.9}Co_{0.1}TiO_3$ $Ba_{0.8}Co_{0.2}TiO_3$ $Ba_{0.7}Co_{0.3}TiO_3$ $Ba_{0.6}Co_{0.4}TiO_3$	400–450	Violet
$Ba_{0.5}Co_{0.5}TiO_3$	420 and 340	Violet and Ultraviolet
$Ba_{0.4}Co_{0.6}TiO_3$ $Ba_{0.3}Co_{0.7}TiO_3$ $Ba_{0.2}Co_{0.8}TiO_3$ $Ba_{0.1}Co_{0.9}TiO_3$ $CoTiO_3$	340	Ultraviolet

3.3. Photocatalytic Application

Experiments were carried out to compare the activities of different $Ba_{(1-x)}Co_{(x)}TiO_3$ photocatalysts on the decolorization rate. Cibacron Brilliant Yellow 3G-P dye cannot be broken down without catalysts when exposed to UV-Vis light. The amount of color removed was estimated by taking absorbance measurements at 365 nm.

Figure 7a presents correlating results comparing the photocatalytic degradation of CBY 3G-P utilizing the photocatalysts $Ba_{1-x}Co_xTiO_3$ under 180 min of irradiation. The absorbance maxima of this dye appear to occur at wavelengths of 267 nm, 292 nm, and 400 nm. The decolorization of the dye solution with $Ba_{1-x}Co_xTiO_3$ catalysts is shown in Figure S7, with kinetic studies every 20 min demonstrated slower photocatalytic reaction rates. This work was repeated for all samples to compare the photocatalytic degradation rates. The sample solutions' starting pH was 5.

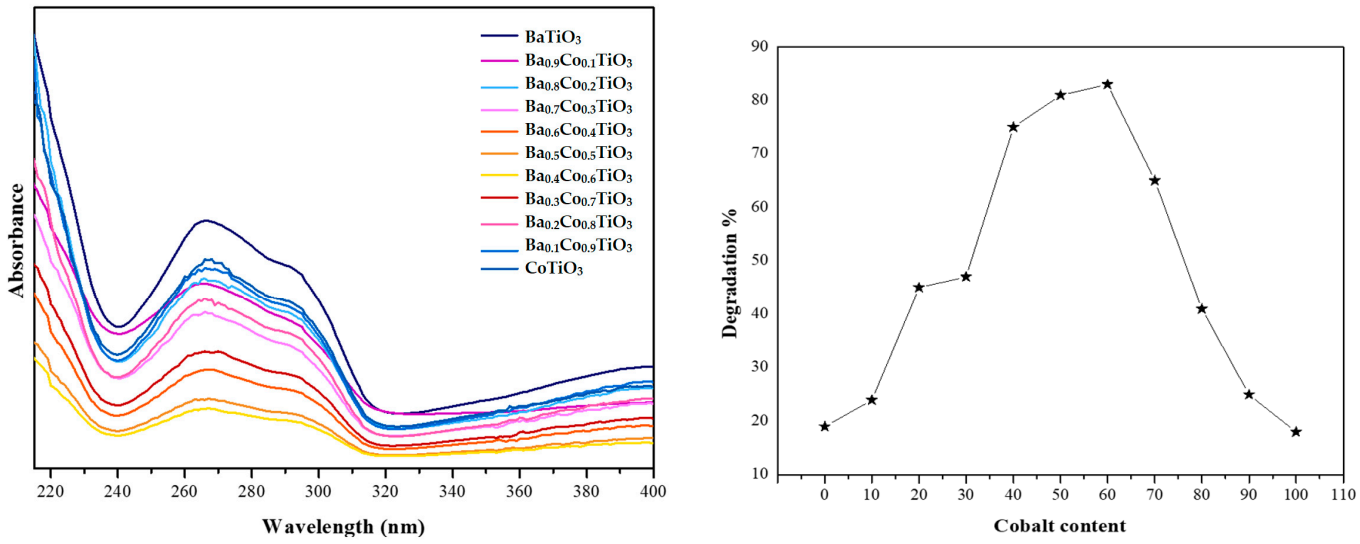

(**a**) (**b**)

Figure 7. (**a**) Photocatalytic degradation rate of CBY3G-P dye over $Ba_{1-x}Co_xTiO_3$ NPs as catalysis under 180 min of irradiation and (**b**) correlation graph showing the variation of photocatalytic degradation of the CBY3G-P as function of cobalt substitution rate.

With 10 ppm of $Ba_{0.4}Co_{0.6}TiO_3$ photocatalysts, the reaction completed at a pH of 4.5 resulted in a 84.61% degradation rate (Figure S7). By checking the PXRD attributed pattern (x = 0.6), we can observe the coexistence of secondary phase $BaCo_9O_{14}$ that generally does not exhibit significant catalytic activity. As observable in similar studies [98,99], this molecule is a magnetic material at room temperature, with interesting electronic transport properties. $BaCo_9O_{14}$ is often used as a reference material to study the magnetic and transport properties of cobalt and oxygen-based materials. The conclusion gathered from this implies that, for the situation of x = 0.6 cobalt substitution rate, this phase does not have a photocatalytic effect on the catalyst, which characterizes the primary phase of composition. The catalyst's dye breakdown rate is significantly accelerated by increasing the cobalt content. This finding suggests that, during photochemical conversion, Co^{2+} is produced from Co^{3+}, providing additional Co^{2+} to interact with H_2O_2 during dye degradation (Equation (3)):

$$Co^{3+} + H_2O + UV \rightarrow \cdot OH + Co^{2+} + H^+ \quad (3)$$

It should be noted that the results presented in this study are consistent with those of a previous study [100]. The results also indicate that the $Ba_{1-x}Co_xTiO_3$ heterostructure has a similar effect on the dye breakdown process (as shown in Figure 7a). For values of x ranging from 0.1 to 0.9, the $Ba_{1-x}Co_xTiO_3$ photocatalysts progressively enhanced the decolorization rate of Cibacron Brilliant Yellow 3G-P dye over a period of 180 min, resulting in degradation efficiencies of 32.93%, 49.20%, 45.61%, 74.39%, 82.08%, 84.61%, 63.67%, 42.94%, and 26.36%, respectively.

As a result, it was revealed that Cibacron Brilliant Yellow 3G-P pollutant degradation efficiency has increased. A drop in degradation efficiency was seen as the catalyst concentration was increased further. This occurs because, once the concentration of photocatalysts rises beyond a certain limit, the solution becomes disordered and UV radiation screens out the reaction, reducing the degradation efficiency. The photocatalytic activity of x = 0.6 showed the maximum degradation efficiency of 84.61% (Figure 7b).

According to the obtained data, the photocatalytic activity of the $Ba_{1-x}Co_xTiO_3$ samples increases as the cobalt concentration rises from x = 0 to x = 0.6. This observation could be explained by the presence of more active sites on the surface of the photocatalysts and the subsequent production of more radicals, such as (−OH).

Typically, in most instances, conduction band (CB) electrons produced by photoexcitation are moved to adsorbed oxygens to create superoxide radical anions ($O_2\bullet-$), while the valence Band (VB) holes oxidize adsorbed water molecules to generate •OH radicals that participate in the degradation of dyes. Furthermore, VB holes created in the semiconductors can also oxidize adsorbed dye molecules into CO_2 and H_2O. However, the actual photocatalytic degradation mechanism can be comprehended based on the relative positioning of the semiconductor VB and CB potentials in relation to $\bullet OH/H_2O$, $O_2/O_2\bullet-$, and the HOMO-LUMO levels of the molecule being degraded. To illustrate the photocatalytic mechanism, energy level diagrams (ELD) are created by calculating the relative band edge positions of the photocatalysts using empirical formulas [100].

$$E_{CB} = \chi(A_aB_bC_c) - 1/2E_g + E^\circ \quad (4)$$

$$E_{VB} = E_{CB} + E_g \quad (5)$$

Calculated results are summarized in Table 9 (below) with:

- χ(Ba) = 2.675 eV, χ(Co) = 4.27 eV, χ(Ti) = 3.455 eV, and χ(O) = 7.54 eV.
- E° = 4.5 eV.

Table 9. Calculated values of valence and conduction band positions of $Ba_{1-x}Co_xTiO_3$ (x = 0, . . . , 1).

Compounds	E_{CB} (eV)	E_{VB} (eV)
$BaTiO_3$	−1.153	2.637
$Ba_{0.9}Co_{0.1}TiO_3$	−0.953	2.537
$Ba_{0.8}Co_{0.2}TiO_3$	−0.884	3.616
$Ba_{0.7}Co_{0.3}TiO_3$	−0.793	2.577
$Ba_{0.6}Co_{0.4}TiO_3$	−0.713	2.597
$Ba_{0.5}Co_{0.5}TiO_3$	−0.562	2.548
$Ba_{0.4}Co_{0.6}TiO_3$	−0.455	2.545
$Ba_{0.3}Co_{0.7}TiO_3$	−0.388	2.582
$Ba_{0.2}Co_{0.8}TiO_3$	−0.325	2.625
$Ba_{0.1}Co_{0.9}TiO_3$	−0.242	2.648
$CoTiO_3$	−0.268	2.782

The energy level diagram (ELD) presented in Figure 8 provides insights into the mechanism of photocatalytic degradation for the sample with a substitution rate of x = 0.6 cobalt, and Supplementary Figure S8 shows ELDs for the rest of the studied samples. The potentials shown in the ELDs are referenced to normal hydrogen electrode (NHE) potentials. From Figure 8, it can be observed that E_{CB} = −0.455 eV is higher than the ($O_2\bullet-$) formation potential of +0.13 eV, which leads to a reduction in the dissolved oxygen required to produce O2•− radicals.

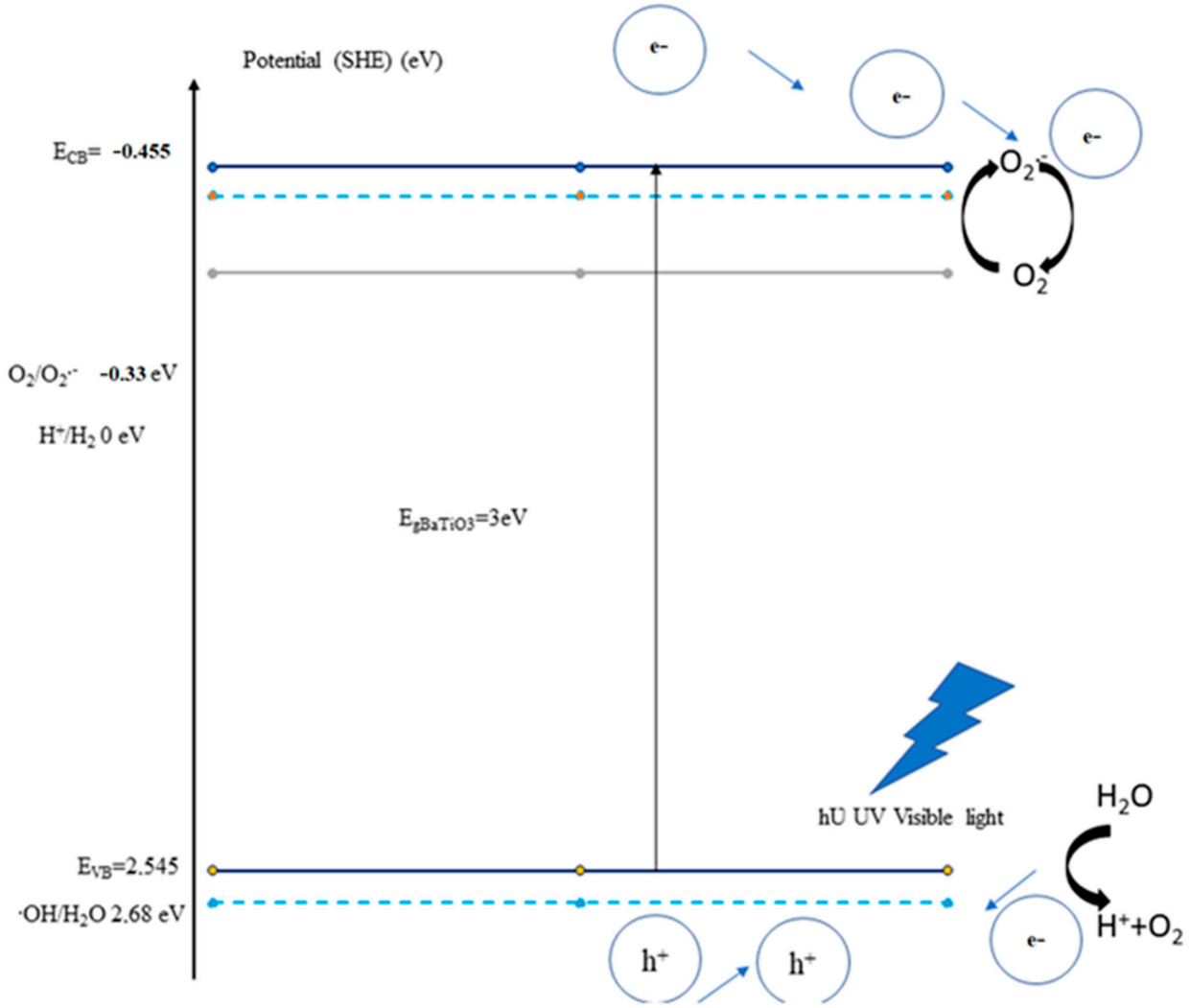

Figure 8. Schematic ELD of $Ba_{0.4}Co_{0.6}TiO_3$ with respect to potential for the generation of ($O_2\bullet-$) ($E^{\circ}(OH/H_2O)$) and $O_2\bullet-$ ($EO_2/O_2\bullet-$) radicals.

Furthermore, the photogenerated VB holes could be transported to the adsorbed dye, leading to its degradation. However, these holes could not form •OH radicals by oxidizing H_2O because of their higher V_B potential (E_{VB} = +2.545 eV vs. NHE) compared to the corresponding E° OH/H_2O potential (E° OH/H_2O = +2.68 eV vs. NHE). The ELD-based proposition is in line with the scavenger test results, indicating O2•− and h^+ as the primary reactive species involved in the degradation of Cibacron Brilliant Yellow 3G-P dye.

4. Conclusions

An investigation of the phase transition, demonstrated by the $BaTiO_3$-$CoTiO_3$ system when the Ba substitution level is increased, and the optical properties in the entire margin of cobalt substitution on the $BaTiO_3$ A-site was performed to enhance the photocatalytic activity. Successful synthesis of the BCT Cobalt ion-substituted barium $Ba_{1-x}Co_xTiO_3$ (x = 0 . . . 1) nanostructure powders was accomplished by destabilizing colloidal solutions. This substitution was assessed using a number of different techniques. A structural analysis was performed using TEM micrographs and confirmed the presence of pseudo-cubic phases ranging in size from 30–114 nm, which is attributable to the tetragonal phase of BCT. This phase is also predominant in the PXRD patterns for x = 0, 0.1, 0.2, and 0.3, indicating high crystallinity in the perovskite structure. As the cobalt concentration increases to x = 0.3, the transition to the isomorphous ilmenite-type rhombohedral CT ceramic phase is

observed, accompanied by the appearance of secondary phases. The Rietveld approach, with an intriguing profile fit that produced lower reliability factors, confirms this logical transition. The unit cell characteristics were reduced by raising the cobalt amount in the BCT nano-compounds series, confirming this effect. The elemental energy dispersive spectroscopy (EDX) of the x = 0.6 confirmed sample, validated the accomplishment of growth, and demonstrated random distributions of cobalt ions. The formed nanoparticles were found to have strong chemical interactions, as revealed by Fourier transform infrared spectroscopy analysis.

Optical tests were performed on the samples to investigate the effects of the A-site replacement rate, and a small red-shift was observed in the absorption curves of BCT compared to pure BT, as detected by PL and UV-visible absorption spectra. The band gap energy of BCT decreased as the barium ion concentration decreased, from 3.7 to 2.8 eV, which enhanced the photocatalytic activity. With a maximum photo-degradation of 84.61% found for x = 0.6, the investigation showed that increasing the quantity of cobalt in the BCT nanoparticles improved the photocatalytic efficiency. As a result, it may be concluded that the catalyst has the potential to selectively degrade dyes in water through photocatalysis.

Supplementary Materials: The following supporting information can be downloaded at: https://www.mdpi.com/article/10.3390/chemengineering7030043/s1, Figure S1: Flow chart of the sol–gel processing of (x = {0, . . . , 1}) powder ceramics. Figure S2: Characteristics and chemical formula of Cibacron Brilliant Yellow 3G-P (Y). Figure S3: Powder X-ray diffraction pattern of synthesized pure BT nanoparticles heated at 1000 °C. Figure S4: Rietveld refinement of synthesized (a) $Ba_{0.9}Co_{0.1}TiO_3$, (b) $Ba_{0.8}Co_{0.2}TiO_3$, (c) $Ba_{0.7}Co_{0.3}TiO_3$, (d) $Ba_{0.6}Co_{0.4}TiO_3$, (e) $Ba_{0.5}Co_{0.5}TiO_3$, (f) $Ba_{0.4}Co_{0.6}TiO_3$, (g) $Ba_{0.3}Co_{0.7}TiO_3$, (h) $Ba_{0.2}Co_{0.8}TiO_3$, (i) $Ba_{0.1}Co_{0.9}TiO_3$, and (j) $CoTiO_3$ structure using Profex BGMN software. Figure S5: TEM micrographs and high-resolution images, respectively, for (a,b) pure BT sample, (c,d) $Ba_{1-x}Co_xTiO_3$ sample with x = 0.2; (e,f) $Ba_{1-x}Co_xTiO_3$ sample with x = 0.4; (i,j) $Ba_{1-x}Co_xTiO_3$ sample with x = 0.8, and (k,l) $Ba_{1-x}Co_xTiO_3$ sample with x = 1($CoTiO_3$ complex). Figure S6: Estimation of band gap energy using Tauc Plot method for $Ba_{1-x}Co_xTiO_3$ {x = 0, . . . , 1} samples; (a) $BaTiO_3$, (b) $Ba_{0.9}Co_{0.1}TiO_3$, (c) $Ba_{0.8}Co_{0.2}TiO_3$, (d) $Ba_{0.7}Co_{0.3}TiO_3$, (e) $Ba_{0.6}Co_{0.4}TiO_3$, (f) $Ba_{0.5}Co_{0.5}TiO_3$, (g) $Ba_{0.3}Co_{0.7}TiO_3$, (h) $Ba_{0.2}Co_{0.8}TiO_3$, (i) $Ba_{0.1}Co_{0.9}TiO_3$, and (j) $CoTiO_3$. Figure S7: Photocatalytic degradation of CBY 3G-P by $Ba_{1-x}Co_xTiO_3$, {x= 0, . . . , 1}: (a) $BaTiO_3$; (b) $Ba_{0.9}Co_{0.1}TiO_3$; (c) $Ba_{0.8}Co_{0.2}TiO_3$; (d) $Ba_{0.7}Co_{0.3}TiO_3$; (e) $Ba_{0.6}Co_{0.4}TiO_3$; (f) $Ba_{0.5}Co_{0.5}TiO_3$; (g) $Ba_{0.4}Co_{0.6}TiO_3$; (h) $Ba_{0.3}Co_{0.7}TiO_3$; (i) $Ba_{0.2}Co_{0.8}TiO_3$; (j) $Ba_{0.1}Co_{0.9}TiO_3$, and (k) $CoTiO_3$ as photocatalyst under 180 min of irradiation. Figure S8: Schematic ELD of $Ba_{1-x}Co_xTiO_3$ with respect to potential for the generation of ($O_2\bullet-$) ($E^\circ_{(OH/H2O)}$) and $O_2\bullet-$ ($E_{O2/O2\bullet-}$) radicals; (a) $BaTiO_3$; (b) $Ba_{0.9}Co_{0.1}TiO_3$; (c) $Ba_{0.8}Co_{0.2}TiO_3$; (d) $Ba_{0.7}Co_{0.3}TiO_3$; (e) $Ba_{0.6}Co_{0.4}TiO_3$; (f) $Ba_{0.5}Co_{0.5}TiO_3$; (g) $Ba_{0.3}Co_{0.7}TiO_3$; (h) $Ba_{0.2}Co_{0.8}TiO_3$; (i) $Ba_{0.1}Co_{0.9}TiO_3$, and (j) $CoTiO_3$.

Author Contributions: Conceptualization, S.J. and W.O.; Formal analysis, S.J. and M.M.; Methodology, S.J. and W.O.; Supervision, W.O.; Validation, C.M., A.B.H.A. and W.O.; Writing—original draft, S.J. and W.O. All authors have read and agreed to the published version of the manuscript.

Funding: This research received no specific grant from any funding agency in the public, commercial, or not-for-profit sectors.

Data Availability Statement: The generated and analyzed data during the current study are included within the article and can be obtained from the corresponding authors upon reasonable request.

Acknowledgments: The results presented are a part of the Ph.D. thesis of Sana Jebali (SJ), realized at LR19ES20: Resources, Materials and Ecosystems (RME), Faculty of Sciences of Bizerte, supervised by Walid Oueslati (WO). SJ acknowledges WO for the original idea of the work, the fruitful discussions about perovskite materials (synthesize and properties), her main contribution, respectively, in the acquisition of experimental results, draft paper writing and the proof reading of the final manuscript.

Conflicts of Interest: The authors declare no conflict of interest.

References

1. Raj, S.; Singh, H.; Bhattacharya, J. Treatment of textile industry wastewater based on coagulation-flocculation aided sedimentation followed by adsorption: Process studies in an industrial ecology concept. *Sci. Total Environ.* **2023**, *857*, 159464. [CrossRef] [PubMed]
2. Araña, J.; Herrera Melián, J.A.; Doña Rodríguez, J.M.; González Díaz, O.; Viera, A.; Pérez Peña, J.; Marrero Sosa, P.M.; Espino Jiménez, V. TiO2-photocatalysis as a tertiary treatment of naturally treated wastewater. *Catal. Today* **2002**, *76*, 279–289. [CrossRef]
3. Coker, E.N.; Lujan-Flores, X.; Donaldson, B.; Yilmaz, N.; Atmanli, A. An Assessment of the Conversion of Biomass and Industrial Waste Products to Activated Carbon. *Energies* **2023**, *16*, 1606. [CrossRef]
4. Abdellatief, M.; AL-Tam, S.M.; Elemam, W.E.; Alanazi, H.; Elgendy, G.M.; Tahwia, A.M. Development of ultra-high-performance concrete with low environmental impact integrated with metakaolin and industrial wastes. *Case Stud. Constr. Mater.* **2023**, *18*, e01724. [CrossRef]
5. Hull, M.S.; Kennedy, A.J.; Steevens, J.A.; Bednar, A.J.; Weiss, C.A., Jr.; Vikesland, P.J. Release of Metal Impurities from Carbon Nanomaterials Influences Aquatic Toxicity. *Environ. Sci. Technol.* **2009**, *43*, 4169–4174. [CrossRef]
6. Yaseen, D.A.; Scholz, M. Textile dye wastewater characteristics and constituents of synthetic effluents: A critical review. *Int. J. Environ. Sci. Technol.* **2019**, *16*, 1193–1226. [CrossRef]
7. Katheresan, V.; Kansedo, J.; Lau, S.Y. Efficiency of various recent wastewater dye removal methods: A review. *J. Environ. Chem. Eng.* **2018**, *6*, 4676–4697. [CrossRef]
8. Lada, Z.G.; Mathioudakis, G.N.; Pavlidou, S.; Goulas, G.; Anastasopoulos, C.; Bokias, G.; Voyiatzis, G.A. Comparative Assessment of the Dyeing Process for Pristine and Modified Cotton Fabrics towards the Reduction of the Environmental Fingerprint. *Sustainability* **2023**, *15*, 3144. [CrossRef]
9. Aye, T.; Anderson, W.A.; Mehrvar, M. Photocatalytic Treatment of Cibacron Brilliant Yellow 3G-P (Reactive Yellow 2 Textile Dye). *J. Environ. Sci. Health Part A* **2003**, *38*, 1903–1914. [CrossRef]
10. Saini, R.D. Textile Organic Dyes: Polluting effects and Elimination Methods from Textile Waste Water. *Inter. J. Chem. Eng. Res.* **2017**, *9*, 121–136.
11. O'Shea, K.E.; Dionysiou, D.D. Advanced Oxidation Processes for Water Treatment. *J. Phys. Chem. Lett.* **2012**, *15*, 2112–2113. [CrossRef]
12. Isopencu, G.O.; Mocanu, A.; Deleanu, I.-M. A Brief Review of Photocatalytic Reactors Used for Persistent Pesticides Degradation. *ChemEngineering* **2022**, *6*, 89. [CrossRef]
13. Nora, S.; Diallo, M.S. Nanomaterials and Water Purification: Opportunities and Challenges. *J. Nanoparticle Res.* **2005**, *7*, 331–342. [CrossRef]
14. Huang, R.; Han, J.W. Improved Catalytic Activity of the High-Temperature Water Gas Shift Reaction on Metal-Exsolved $La_{0.}$ 9Ni0. 05$Fe_{0.\ 95}O_3$ by Controlling Reduction Time. *ChemEngineering* **2021**, *5*, 28. [CrossRef]
15. Bano, K.; Kaushal, S.; Singh, P.P. A review on photocatalytic degradation of hazardous pesticides using heterojunctions. *Polyhedron* **2021**, *209*, 115465. [CrossRef]
16. Sun, B.; Zhou, G.; Sun, L.; Zhao, H.; Chen, Y.; Yang, F.; Song, Q. ABO $_3$ multiferroic perovskite materials for memristive memory and neuromorphic computing. *Nanoscale Horiz.* **2021**, *6*, 939–970. [CrossRef]
17. Kovalenko, M.V.; Protesescu, L.; Bodnarchuk, M.I. Properties and potential optoelectronic applications of lead halide perovskite nanocrystals. *Science* **2017**, *750*, 745–750. [CrossRef]
18. Fu, P.; Shan, Q.; Shang, Y.; Song, J.; Zeng, H.; Ning, Z.; Gong, J. Perovskite nanocrystals: Synthesis, properties and applications. *Sci. Bull.* **2017**, *62*, 369–380. [CrossRef] [PubMed]
19. Lemziouka, H.; Nekkach, F.; Boutahar, A.; Moubah, R.; Omari, L.H.; Filali, M.; El Yazidi, M. Effect of Cobalt Doping on the Structural, Linear, and Nonlinear Optical Properties in $Ba_{1-x}Co_x$ TiO_3 Perovskites. *J. Electron. Mater.* **2023**, *52*, 3420–3430. [CrossRef]
20. Plyushch, A.; Macutkevič, J.; Sokal, A.; Lapko, K.; Kudlash, A.; Adamchuk, D.; Ksenevich, V.; Bychanok, D.; Selskis, A.; Kuzhir, P.; et al. The Phosphate-Based Composite Materials Filled with Nano-Sized $BaTiO_3$ and Fe_3O_4: Toward the Unfired Multiferroic Materials. *Materials* **2021**, *14*, 133. [CrossRef]
21. Peraza, J.; Bocanegra, E.H.; Tello, M.J.; Fernandez, J. Thermal properties of $BaTiO_3$ crystals doped with cobalt. *Mater. Res. Bull.* **1976**, *11*, 981–984. [CrossRef]
22. Yu, S.W.; Yeh, W.C.V.; Jou, J.L.; Lei, C.M. Synthesis and characterization the dielectric properties of cobalt doping hexagonal $BaTiO_3$. *Ferroelectrics* **2013**, *456*, 31–37. [CrossRef]
23. Fernandez, J.F.; Duran, P.; Moure, C. Microstructure and dielectric properties of $BaTiO_3$ doped with niobium and cobalt. *Ferroelectrics* **1992**, *127*, 53–58. [CrossRef]
24. Bujakiewicz-Koronska, R.; Gondek, Ł.; Vasylechko, L.; Balanda, M.; Juszynska-Galazka, E.; Galazka, M.; Nakazawa, Y. Magnetoelectric, spectroscopic, optical and elastic properties of Co-doped $BaTiO_3$ ceramics. *J. Alloy. Compd.* **2023**, *946*, 169344. [CrossRef]
25. Bujakiewicz-Koronska, R.; Vasylechko, L.; Markiewicz, E.; Nalecz, D.M.; Kalvane, A. X-ray and dielectric characterization of Co doped tetragonal $BaTiO_3$ ceramics. *Phase Transit.* **2017**, *90*, 78–85. [CrossRef]
26. Zhuravlev, V.A.; Minin, R.V.; Itin, V.I. Multiferrroics of (1–x) $BaFe_{12}O_{19}$–x$BaTiO_3$ and (1–x) $CoFe_2O_4$–xPb $(Zr_{0.53}Ti_{0.47})$ O_3 Compositions with a Template Structure. *Russ. Phy. J.* **2023**, *65*, 2170–2181. [CrossRef]

27. Etier, M.; Gao, Y.; Shvartsman, V.V.; Elsukova, A.; Landers, J.; Wende, H.; Lupascu, D.C. Cobalt ferrite/barium titanate core/shell nanoparticles. *Ferroelectrics* **2012**, *438*, 115–122. [CrossRef]
28. Rani, A.; Kolte, J.; Gopalan, P. Effect of Cobalt substitution on the structural, electrical and magnetic properties of $BaTiO_3$ ceramics. In Proceedings of the Joint IEEE International Symposium on the Applications of Ferroelectric (ISAF), International Symposium on Integrated Functionalities (ISIF), and Piezoelectric Force Microscopy Workshop (PFM), Singapore, 24–27 May 2015. [CrossRef]
29. Tihtih, M.; Sevostianova, I.N.; Kurovics, E.; Sablina, T.Y.; Kulkov, S.N.; Gömze, L.A. Examination of the influence of cobalt substitution on the properties of barium titanate ceramics. *Epitoanyag-J. Silic. Based Compos. Mater.* **2021**, *73*, 160–165. [CrossRef]
30. Ul, R.; Marchet, P.; Pham-Thi, M.; Tran-Huu-Hue, L.P. Improved properties of doped $BaTiO_3$ piezoelectric ceramics. *Phy. Status Solidi* **2019**, *216*, 1900413. [CrossRef]
31. Yang, L.; Qiu, H.; Pan, L.; Guo, Z.; Xu, M.; Yin, J.; Zhao, X. Magnetic properties of $BaTiO_3$ and $BaTi_{1-x}M_xO_3$ (M = Co, Fe) nanocrystals by hydrothermal method. *J. Magn. Magn. Mater.* **2014**, *350*, 1–5. [CrossRef]
32. Osoro, G.M.; Bregiroux, D.; Thi, M.P.; Levassort, F. Structural and piezoelectric properties evolution induced by cobalt doping and cobalt/niobium co-doping in $BaTiO_3$. *Mater. Lett.* **2016**, *166*, 259–262. [CrossRef]
33. Yang, Y.; Hao, H.; Zhang, L.; Chen, C.; Luo, Z.; Liu, Z.; Liu, H. Structure, electrical and dielectric properties of Ca substituted $BaTiO_3$ ceramics. *Ceram. Int.* **2018**, *44*, 11109–11115. [CrossRef]
34. Maikhuri, N.; Panwar, A.K.; Jha, A.K. Investigation of A-and B-site Fe substituted $BaTiO_3$ ceramics. *J. Appl. Phys.* **2013**, *113*, 17D915. [CrossRef]
35. Kishi, H.; Kohzu, N.; Iguchi, Y.; Sugino, J.; Kato, M.; Ohsato, H.; Okuda, T. Occupational sites and dielectric properties of rare-earth and Mn substituted $BaTiO_3$. *J. Eur. Ceram. Soc.* **2001**, *21*, 1643–1647. [CrossRef]
36. Verma, K.C.; Kotnala, R.K. Multiferroic approach for Cr, Mn, Fe, Co, Ni, Cu substituted $BaTiO_3$ nanoparticles. *Mater. Res. Express* **2016**, *3*, 055006. [CrossRef]
37. Tihtih, M.; Ibrahim, J.E.F.; Basyooni, M.A.; Kurovics, E.; Belaid, W.; Hussainova, I.; Kocserha, I. Role of A-site (Sr), B-site (Y), and A, B sites (Sr, Y) substitution in lead-free $BaTiO_3$ ceramic compounds: Structural, optical, microstructure, mechanical, and thermal conductivity properties. *Ceram. Int.* **2023**, *49*, 1947–1959. [CrossRef]
38. Kullmer, R. Dielectric and ferroelectric properties of pulsed-laser deposited $BaTiO_3$ films. *Appl. Phys. A* **1997**, *65*, 273–279. [CrossRef]
39. Zhu, J.; Li, H.; Zhong, L.; Xiao, P.; Xu, X.; Yang, X.; Zhao, Z.; Li, J. Perovskite oxides: Preparation, characterizations, and applications in heterogeneous catalysis. *ACS Catal.* **2014**, *4*, 2917–2940. [CrossRef]
40. Peña, M.A.; Fierro, J.L.G. Chemical structures and performance of perovskite oxides. *Chem. Rev.* **2001**, *101*, 1981–2017. [CrossRef]
41. Zhang, S.; Chen, D.; Liu, Z.; Ruan, M.; Guo, Z. Novel strategy for efficient water splitting through pyro-electric and pyro-photo-electric catalysis of $BaTiO_3$ by using thermal resource and solar energy. *Appl. Catal. B Environ.* **2021**, *284*, 119686. [CrossRef]
42. Pattanayak, P.; Singh, P.; Bansal, N.K.; Paul, M.; Dixit, H.; Porwal, S.; Mishra, S.; Singh, T. Recent progress in perovskite transition metal oxide-based photocatalyst and photoelectrode materials for solar-driven water splitting. *J. Environ. Chem. Eng.* **2022**, *10*, 108429. [CrossRef]
43. Zhang, M.; Jeerh, G.; Zou, P.; Lan, R.; Wang, M.; Wang, H.; Tao, S. Recent development of perovskite oxide-based electrocatalysts and their applications in low to intermediate temperature electrochemical devices. *Mater. Today* **2021**, *49*, 351–377. [CrossRef]
44. Shen, H.; Xia, K.; Wang, P. The electronic, structural, ferroelectric and optical properties of strontium and zirconium co-doped $BaTiO_3$. *Solid State Commun.* **2022**, *355*, 114930. [CrossRef]
45. You, H.; Li, S.; Fan, Y.; Guo, X.; Lin, Z.; Ding, R.; Cheng, X.; Zhang, H.; Lo, T.W.B.; Hao, J.; et al. Accelerated pyro-catalytic hydrogen production enabled by plasmonic local heating of Au on pyroelectric BaTiO3 nanoparticles. *Nat. Commun.* **2022**, *13*, 6144. [CrossRef]
46. Noh, B.I.; Yang, S.C. Ferromagnetic, ferroelectric, and magnetoelectric properties in individual nanotube-based magnetoelectric films of $CoFe_2O_4/BaTiO_3$ using electrically resistive core-shell magnetostrictive nanoparticles. *J. Alloy. Compd.* **2022**, *891*, 161861. [CrossRef]
47. Hossain, S.; Hossain, S. Magnetic and Optical Characterization of Cobalt Ferrite–Barium Titanate Core–Shell for Biomedical Applications. *IEEE Trans. Magn.* **2021**, *58*, 1–8. [CrossRef]
48. Sunarso, J.; Hashim, S.S.; Zhu, N.; Zhou, W. Perovskite oxides applications in high temperature oxygen separation, solid oxide fuel cell and membrane reactor: A review. *Prog. Energy Combust. Sci.* **2017**, *61*, 57–77. [CrossRef]
49. Ertuğ, B. The overview of the electrical properties of barium titanate. *Am. J. Eng. Res.* **2013**, *2*, 1–7.
50. Duong, N.X.; Bae, J.S.; Jeon, J.; Lim, S.Y.; Oh, S.H.; Ullah, A.; Kim, T.H. Polymorphic phase transition in $BaTiO_3$ by Ni doping. *Ceram. Int.* **2019**, *45*, 16305–16310. [CrossRef]
51. Shuai, Y.; Zhou, S.; Bürger, D.; Reuther, H.; Skorupa, I.; John, V.; Schmidt, H. Decisive role of oxygen vacancy in ferroelectric versus ferromagnetic Mn-doped $BaTiO_3$ thin films. *J. Appl. Phys.* **2011**, *109*, 084105. [CrossRef]
52. Guo, Z.; Pan, L.; Bi, C.; Qiu, H.; Zhao, X.; Yang, L.; Rafique, M.Y. Structural and multiferroic properties of Fe-doped $Ba_{0.5}Sr_{0.5}TiO_3$ solids. *J. Magn. Magn. Mater.* **2013**, *325*, 24–28. [CrossRef]
53. Chen, J.; Deng, H.; Pan, Y.; Zheng, D.; Sun, L.; Tao, J.; Chu, J. Band gap modulation and improved magnetism of double perovskite Sr_2KMoO_6 (K = Fe, Co, Ni, Mn) doped $BaTiO_3$ ceramics. *Ceram. Int.* **2022**, *48*, 7629–7635. [CrossRef]

54. Feng, M.; Wang, J.; Hu, J.-M.; Wang, J.; Ma, J.; Li, H.-B.; Shen, Y.; Lin, Y.-H.; Chen, L.-Q.; Nan, C.-W. Optimizing direct magnetoelectric coupling in Pb(Zr,Ti)O3/Ni multiferroic film heterostructures. *Appl. Phys. Lett.* **2015**, *106*, 72901. [CrossRef]
55. Jayanthi, S.; Kutty, T.R.N. Dielectric properties of 3d transition metal substituted $BaTiO_3$ ceramics containing the hexagonal phase formation. *J. Mater. Sci. Mater. Electron.* **2008**, *19*, 615–626. [CrossRef]
56. Dawson, J.A.; Freeman, C.L.; Harding, J.H.; Sinclair, D.C. Phase stabilisation of hexagonal barium titanate doped with transition metals: A computational study. *J. Solid State Chem.* **2013**, *200*, 310–316. [CrossRef]
57. Yadav, K.; Singh, M.P.; Razavi, F.S.; Varma, G.D. Effect of A-site cation size on magnetic and charge-ordering properties of $Ln_{0.5}Sr_{0.5}Mn_{0.9}Cu_{0.1}O_3$ (Ln = La, Pr, Nd, or Ho). *Mater. Sci. Eng. B* **2012**, *177*, 1225–1231. [CrossRef]
58. Taheri, M.; Maaref, S.; Kantzas, A.; Bryant, S.; Trudel, S. Improving the colloidal stability of PEGylated $BaTiO_3$ nanoparticles with surfactants. *Chem. Phys.* **2023**, *564*, 111701. [CrossRef]
59. Abdullah, H.; Abdullah, N.A.; Zulfakar, M.S.; Wan Jalal, W.N. Fabrication of Nanostructure $Ba_{(1-x)}Co_{(x)}$ TiO_3 thin Films Synthesized by Sol-Gel Method for Patch Antenna Application. In *Developments in Strategic Materials and Computational Design V: A Collection of Papers, Proceedings of the 38th International Conference on Advanced Ceramics and Composites, Daytona Beach, FL, USA, 27–31 January 2014*; John Wiley & Sons, Inc.: Hoboken, NJ, USA, 2014; Volume 35, pp. 189–199. [CrossRef]
60. Mi, L.; Zhang, Q.; Wang, H.; Wu, Z.; Guo, Y.; Li, Y.; Qi, X. Synthesis of $BaTiO_3$ nanoparticles by sol-gel assisted solid phase method and its formation mechanism and photocatalytic activity. *Ceram. Int.* **2020**, *46*, 10619–10633. [CrossRef]
61. Pierre, A.C. *Introduction to Sol-Gel Processing*, 1st ed.; Springer Nature: Berlin/Heidelberg, Germany, 2020; pp. 1–700.
62. Doebelin, N.; Kleeberg, R. Profex: A graphical user interface for the Rietveld refinement program BGMN. *J. Appl. Crystallogr.* **2015**, *48*, 1573–1580. [CrossRef]
63. Schanze, K.S.; Kamat, P.V.; Yang, P.; Bisquert, J. Progress in perovskite photocatalysis. *ACS Energy Lett.* **2020**, *5*, 2602–2604. [CrossRef]
64. Won, S.W.; Yun, Y.S. Biosorptive removal of Reactive Yellow 2 using waste biomass from lysine fermentation process. *Dyes Pigments* **2008**, *76*, 502–507. [CrossRef]
65. Natarajan, S.; Bajaj, H.C.; Tayade, R.J. Recent advances based on the synergetic effect of adsorption for removal of dyes from waste water using photocatalytic process. *J. Environ. Sci.* **2018**, *65*, 201–222. [CrossRef]
66. Sakkas, V.A.; Islam, M.A.; Stalikas, C.; Albanis, T.A. Photocatalytic degradation using design of experiments: A review and example of the Congo red degradation. *J. Hazard. Mater.* **2010**, *175*, 33–44. [CrossRef] [PubMed]
67. Jia, Z.; Miao, J.; Lu, H.B.; Habibi, D.; Zhang, W.C.; Zhang, L.C. Photocatalytic degradation and absorption kinetics of cibacron brilliant yellow 3G-P by nanosized ZnO catalyst under simulated solar light. *J. Taiwan Inst. Chem. Eng.* **2016**, *60*, 267–274. [CrossRef]
68. Alshamsi, H.A.; Hussein, B.S. Synthesis, characterization and photocatalysis of γ-Fe_2O_3 nanoparticles for degradation of Cibacron Brilliant Yellow 3G-P. *Asian J. Chem.* **2018**, *30*, 273–279. [CrossRef]
69. Miao, J.; Zhang, R.; Zhang, L. Photocatalytic degradations of three dyes with different chemical structures using ball-milled TiO_2. *Mater. Res. Bull.* **2018**, *97*, 109–114. [CrossRef]
70. Ammar, S.H.; Elaibi, A.I.; Mohammed, I.S. Core/shell Fe_3O_4@ Al_2O_3-PMo magnetic nanocatalyst for photocatalytic degradation of organic pollutants in an internal loop airlift reactor. *J. Water Process Eng.* **2020**, *37*, 101240. [CrossRef]
71. Alshamsi, H.A.H.; Hussein, B.S. Hydrothermal preparation of silver doping zinc oxide nanoparticles: Study the characterization and photocatalytic activity. *Orient. J. Chem.* **2018**, *34*, 1898. [CrossRef]
72. Rovani, S.; Fernandes, A.N.; Prola, L.D.; Lima, E.C.; Santos, W.O.; Adebayo, M.A. Removal of Cibacron Brilliant Yellow 3G-P Dye from aqueous solutions by Brazilian peats as biosorbents. *Chem. Eng. Commun.* **2014**, *201*, 1431–1458. [CrossRef]
73. Jia, Z.; Zhang, W.C.; Wang, W.M.; Habibi, D.; Zhang, L.C. Amorphous Fe78Si9B13 alloy: An efficient and reusable photo-enhanced Fenton-like catalyst in degradation of cibacron brilliant red 3B-A dye under UV–vis light. *Appl. Catal. B Environ.* **2016**, *192*, 46–56. [CrossRef]
74. Vicas, C.S.; Namratha, K.; Nayan, M.B.; Byrappa, K. Controlled Hydrothermal Synthesis of Bismuth Vanadate Nano-articulate Structures: Photooxidation of Methicillin Resistant Staphylococcus aureus and Organic Dyes. *Mater. Today Proc.* **2019**, *9*, 468–480. [CrossRef]
75. Radia, D.; Fouzia, T.; Rachida, R.; Wahib, N.M.; Bentahar, F. Photocatalysis process to treat polluted water by azo dye Cibacron Brilliant Yellow 3G-P. *Water Sci. Technol.* **2022**, *86*, 1774–1789. [CrossRef]
76. Amaechi, I.C.; Youssef, A.H.; Kolhatkar, G.; Rawach, D.; Gomez-Yañez, C.; Claverie, J.P.; Ruediger, A. Ultrafast microwave-assisted hydrothermal synthesis and photocatalytic behaviour of ferroelectric Fe^{3+}-doped $BaTiO_3$ nanoparticles under simulated sunlight. *Catal. Today* **2021**, *360*, 90–98. [CrossRef]
77. Senthilkumar, P.; Jency, D.A.; Kavinkumar, T.; Dhayanithi, D.; Dhanuskodi, S.; Umadevi, M.; Jothivenkatachalam, K. Built-in electric field assisted photocatalytic dye degradation and photoelectrochemical water splitting of ferroelectric Ce doped $BaTiO_3$ nanoassemblies. *ACS Sustain. Chem. Eng.* **2019**, *7*, 12032–12043. [CrossRef]
78. Srilakshmi, C.; Saraf, R.; Prashanth, V.; Rao, G.M.; Shivakumara, C. Structure and catalytic activity of Cr-doped $BaTiO_3$ nanocatalysts synthesized by conventional oxalate and microwave assisted hydrothermal methods. *Inorg. Chem.* **2016**, *55*, 4795–4805. [CrossRef] [PubMed]
79. Srilakshmi, C.; Rao, G.M.; Saraf, R. Effect of the nature of a transition metal dopant in $BaTiO_3$ perovskite on the catalytic reduction of nitrobenzene. *RSC Adv.* **2015**, *5*, 45965–45973. [CrossRef]

80. Yang, B.; Chen, H.; Yang, Y.; Wang, L.; Bian, J.; Liu, Q.; Lou, X. Insights into the tribo-/pyro-catalysis using Sr-doped $BaTiO_3$ ferroelectric nanocrystals for efficient water remediation. *Chem. Eng. J.* **2021**, *416*, 128986. [CrossRef]
81. Alkathy, M.S.; Eiras, J.A.; Zabotto, F.L.; Raju, K.J. Structural, optical, dielectric, and multiferroic properties of sodium and nickel co-substituted barium titanate ceramics. *J. Mater. Sci. Mater. Electron.* **2021**, *32*, 12828–12840. [CrossRef]
82. Liebermann, R.C. Elasticity of the ilmenite-perovskite phase transformation in $CdTiO_3$. *Earth Planet. Sci. Lett.* **1976**, *29*, 326–332. [CrossRef]
83. Navrotsky, A. Energetics and crystal chemical systematics among ilmenite, lithium niobate, and perovskite structures. *Chem. Mater.* **1998**, *10*, 2787–2793. [CrossRef]
84. Susaki, J.I. CdGeO3-phase transformations at high pressure and temperature and structural refinement of the perovskite polymorph. *Phys. Chem. Miner.* **1989**, *16*, 634–641. [CrossRef]
85. Kuroda, K.; Irifune, T.; Inoue, T.; Nishiyama, N.; Miyashita, M.; Funakoshi, K.; Utsumi, W. Determination of the phase boundary between ilmenite and perovskite in MgSiO 3 by in situ X-ray diffraction and quench experiments. *Phys. Chem. Miner.* **2000**, *27*, 523–532. [CrossRef]
86. Yamazaki, D.; Ito, E.; Tange, Y.; Yoshino, T.; Zhai, S.; Fukui, H.; Funakoshi, K.I. Phase boundary between ilmenite and perovskite structures in $MnGeO_3$ determined by in situ X-ray diffraction measurements. *Phys. Chem. Miner.* **2007**, *34*, 269–273. [CrossRef]
87. Patterson, A.L. The Scherrer formula for X-ray particle size determination. *Phys. Rev.* **1939**, *56*, 978. [CrossRef]
88. Bormanis, K.; Kalvane, A.; Burkhanov, A.I.; Eglite, L.; Dikov, R.V. Dielectric and acoustic properties of modified barium titanate ceramics. *Ferroelectrics* **2019**, *538*, 12–19. [CrossRef]
89. Wang, S.; Tang, S.; Gao, H.; Chen, X.; Liu, H.; Yu, C.; Yang, H. Microstructure, optical, photoluminescence properties and the intrinsic mechanism of photoluminescence and photocatalysis for the $BaTiO_3$, $BaTiO_3/TiO_2$ and $BaTiO_3/TiO_2/CeO_2$ smart composites. *Opt. Mater.* **2021**, *118*, 111273. [CrossRef]
90. Darwish, A.G.A.; Badr, Y.; El Shaarawy, M.; Shash, N.M.H.; Battisha, I. KInfluence of the Nd^{3+} ions content on the FTIR and the visible up-conversion luminescence properties of nano-structure $BaTiO_3$, prepared by sol–gel technique. *J. Alloy. Compd.* **2010**, *489*, 451–455. [CrossRef]
91. Baiju, K.G.; Nagarajan, A.; Marappa Gounder Sadasivam, A.; Sukumar Rajan, D.D.; Sri Sai Vignathi, K.; Balu, M.; Kumaresan, D. Hydrothermal synthesis, dielectric properties of barium titanate, cobalt doped barium titanate, and their graphene nanoplatelet composites. *Asia-Pac. J. Chem. Eng.* **2020**, *15*, e2550. [CrossRef]
92. Myrick, M.L.; Simcock, M.N.; Baranowski, M.; Brooke, H.; Morgan, S.L.; McCutcheon, J.N. The Kubelka-Munk diffuse reflectance formula revisited. *Appl. Spectrosc. Rev.* **2011**, *46*, 140–165. [CrossRef]
93. Makuła, P.; Pacia, M.; Macyk, W. How to correctly determine the band gap energy of modified semiconductor photocatalysts based on UV–Vis spectra. *J. Phys. Chem. Lett.* **2018**, *9*, 6814–6817. [CrossRef]
94. Cardona, M. Optical properties and band structure of $SrTiO_3$ and $BaTiO_3$. *Phy. Rev.* **1965**, *140*, A651–A655. [CrossRef]
95. Shihab, N.K. Cavity enhancement in nonlinear absorption and photoluminescence of $BaTiO_3$. *Optik* **2020**, *207*, 163896. [CrossRef]
96. Hasan, M.; Hossain, A.A. Structural, electronic and optical properties of strontium and nickel co-doped $BaTiO_3$: A DFT based study. *Comput. Condens. Matter* **2021**, *28*, e00578. [CrossRef]
97. Dudnikov, V.A.; Orlov, Y.S.; Gavrilkin, S.Y.; Gorev, M.V.; Vereshchagin, S.N.; Solovyov, L.A.; Ovchinnikov, S.G. Effect of Gd and Sr ordering in A sites of doped $Gd_{0.2}Sr_{0.8}CoO_{3-\delta}$ perovskite on its structural, magnetic, and thermodynamic properties. *J. Phys. Chem. C* **2016**, *120*, 13443–13449. [CrossRef]
98. Sabyasachi, S.; Majumdar, S.; Giri, S. Field induced phase transition in Sm 0.5 $(Ca_{1-x}Sr_x)_{0.5}$ MnO_3. *AIP Conf. Proc.* **2014**, *1591*, 1539–1540. [CrossRef]
99. Tong, P.; Yu, J.; Huang, Q.; Yamada, K.; Louca, D. Possible Link of a Structurally Driven Spin Flip Transition and the Insulator-Metal Transition in the Perovskite $La_{1-x}Ba_x$ CoO_3. *Phys. Rev. Lett.* **2011**, *106*, 156407. [CrossRef] [PubMed]
100. Naresh, G.; Malik, J.; Meena, V.; Mandal, T.K. pH-mediated collective and selective solar photocatalysis by a series of layered Aurivillius perovskites. *ACS Omega* **2018**, *3*, 11104–11116. [CrossRef]